

**HOT DEFORMATION BEHAVIOUR AND PROCESSING MAPS OF HIGH CARBON
LOW ALLOY STEEL**

A DISSERTATION

*Submitted in the partial fulfilment of the
requirements for the award of the degree*

of

MASTER IN TECHNOLOGY

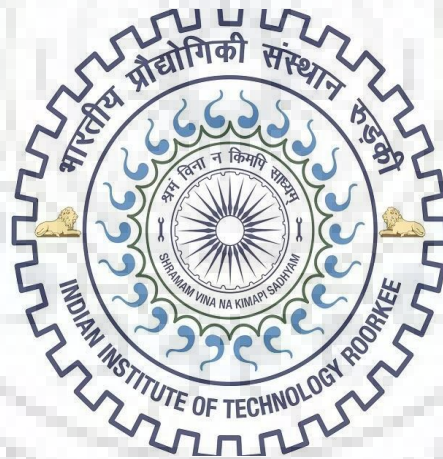
in

METALLURGICAL AND MATERIALS ENGINEERING

(with specialisation in Industrial Metallurgy)

By

DEEPAK KUMAR



SESSION (2016-2018)

DEPARTMENT OF METALLURGICAL AND MATERIALS ENGINEERING

INDIAN INSTITUTE OF TECHNOLOGY ROORKEE

MAY 2018

INDIAN INSTITUTE OF TECHNOLOGY, ROORKEE

CANDIDATE'S DECLARATION

I hereby certify that the work which is being presented in the dissertation, entitled “**STUDY ON HOT DEFORMATION BEHAVIOUR AND PROCESSING MAPS OF HIGH CARBON LOW ALLOY STEEL**” in partial fulfilment of Master of Technology in the **Department of Metallurgical and Materials Engineering** with specialization in “**Industrial Metallurgy**”, **Indian Institute of Technology Roorkee**, is an authentic record of my own work carried out during the period from May,2017 to May,2018 under the supervision of **Dr. S. K. Nath**, Professor, Department of Metallurgical and Materials Engineering, Indian Institute of Technology Roorkee.

The matter embodied in the dissertation has not been submitted to any University/Institute for award of any other degree.

Date:

Place:

(DEEPAK KUMAR)

(16544005)

CERTIFICATE

This is to certify that the above statement made by the candidate is correct to the best of my knowledge.

(Dr. S. K. Nath)

Professor MMED, IIT Roorkee

ABSTRACT

Manufacturers always try to reduce the cost of raw material and production without the loss of quality. Thermomechanical processing and deformation study at elevated temperatures can control the process parameters which results in improved mechanical properties of material. Review of literature shows that there is a need to perform more hot deformation studies in widest range of processing parameters for high carbon low alloy steels which find large number of applications in automobile industry, springs used for shock absorber, tyre cords, bolts, ball bearings, bridge cables, piano wire etc.

In the present study hot deformation behaviour of high carbon low alloy steel has been studied using thermomechanical simulator Gleeble[®] 3800. The tests were carried out in temperature range from 850°C-1100°C and strain rate 0.01 s⁻¹ to 10 s⁻¹. Constitutive analysis is done to model the flow behaviour by calculating Zener Hollomon parameter and flow stress values are predicted. Microstructure evolution after the hot deformation at different temperatures and strain rate is studied. Processing maps are drawn based on different models, flow localization parameters and constitutive equations. Different processing maps based on different instability criteria were plotted and compared to find the optimum workability region. A multilayer Artificial Neural Network (ANN) with feed forward back propagation and having ten neurons in hidden layer is trained to predict the flow stress. A comparative study is done between constitutive equations modelling and ANN modelling. Further, initiation and evolution of dynamic recrystallization is studied from the experimentally obtained flow curves. Strain for onset of dynamic recrystallisation i.e. critical strain was derived from strain hardening rate vs stress curve. The variation of critical strain with peak strain was established. The extent of dynamic recrystallisation was found using the Avrami model and it was found that this model shows good agreement with experimental data.

ACKNOWLEDGEMENTS

Firstly, I would like to express my deepest gratitude, profound indebtedness, deepest respect and heartiest thanks to my supervisor Dr. S. K. Nath (Prof.) Department of Metallurgical and Materials Engineering (MMED), Indian Institute of Technology, Roorkee, for his valuable supervision and encouragement throughout the completion of my M.Tech dissertation work. His continuous suggestions and encouragement is valuable. The words are not sufficient to express my heartfelt thanks and feelings to my mentor for his valuable guidance, support and belief in me.

Now I would like to express my sincere thanks to Ph.D scholar Mr. Sumit Kumar for his immense support and help to complete my M.Tech dissertation work.

Now I would like to express my sincere thanks to Mr. Rajendra Sharma and Mr. Naresh for their help and support towards completion of my dissertation work. I would like to thank technical and administrative staffs of the MMED who helped me in all possible ways during my M.Tech work.

Finally I express my heartiest gratitude to my parents for their unflagging love and support throughout my life. I am also indebted to my sister for her timely valuable advices, care and love throughout the life.

Above all, I express my gratitude from the core of my heart to God for giving courage, strength and patience to carry out my research work.

(DEEPAK KUMAR)

Table of Contents

Candidate's Declaration.....	i
Abstract.....	ii
Acknowledgement.....	iii
Table of contents.....	iv
List of Figures.....	vi
List of Symbols.....	ix
CHAPTER 1 Introduction.....	1
1.1 Hot workability and processing maps.....	2
1.2 Artificial Neural Network Modelling.....	3
1.3 Determination of critical conditions of Dynamic recrystallisation.....	3
CHAPTER 2 Literature review.....	4
2.1 Hot deformation of Steels.....	4
2.2 Hot Deformation.....	6
2.3 Deformation mechanisms.....	6
2.4 Strain hardening mechanism.....	7
2.5 Softening mechanism.....	7
2.6 Workability and its evaluation.....	7
2.7 Materials modelling in hot deformation.....	8
2.7.1 Kinetic model.....	8
2.7.2 Atomistic models- Raj maps.....	8
2.7.3 Dynamic materials model.....	9
2.7.4 Other models.....	9
2.8 Research gap.....	10
2.9 Problem formulation.....	11

CHAPTER 3	Experimental Methodology.....	12
3.1	Procurement of the material.....	12
3.2	Sample preparation.....	12
3.3	Dilatometry test.....	13
3.4	Uniaxial compression test.....	13
3.5	Gleeble® 3800 Thermo-mechanical simulator.....	14
3.6	Microstructural characterization.....	16
3.7	Measurement of Hardness.....	17
CHAPTER 4	Theory and analysis.....	18
4.1	Processing maps.....	18
4.2	Basic constitutive equations.....	20
4.3	Zenner-Holloman parameter.....	21
CHAPTER 5	Results and discussion.....	22
5.1	Initial characterization.....	22
5.2	True Stress Stress Strain curves.....	23
5.3	Correction for Adiabatic Temperature Rise.....	26
5.4	Constitutive Equation analysis.....	29
5.5	Prediction of flow Stress.....	30
5.6	Processing maps.....	35
5.6.1	Maps based on Dynamic Materials Model (DMM).....	35
5.7	Characterization of the hot deformed specimen.....	38
CHAPTER 6	Artificial Neural Networks.....	42
6.1	Results of ANN modelling.....	43
CHAPTER 7	Determination of critical conditions for Dynamic Recrystallisation.....	48
7.1	Strain for maximum dynamic softening.....	49

7.2	Extent of Dynamic Recrystallisation.....	51
CHAPTER 8	Summary	54
CHAPTER 9	Future scope of work.....	56
References:	57

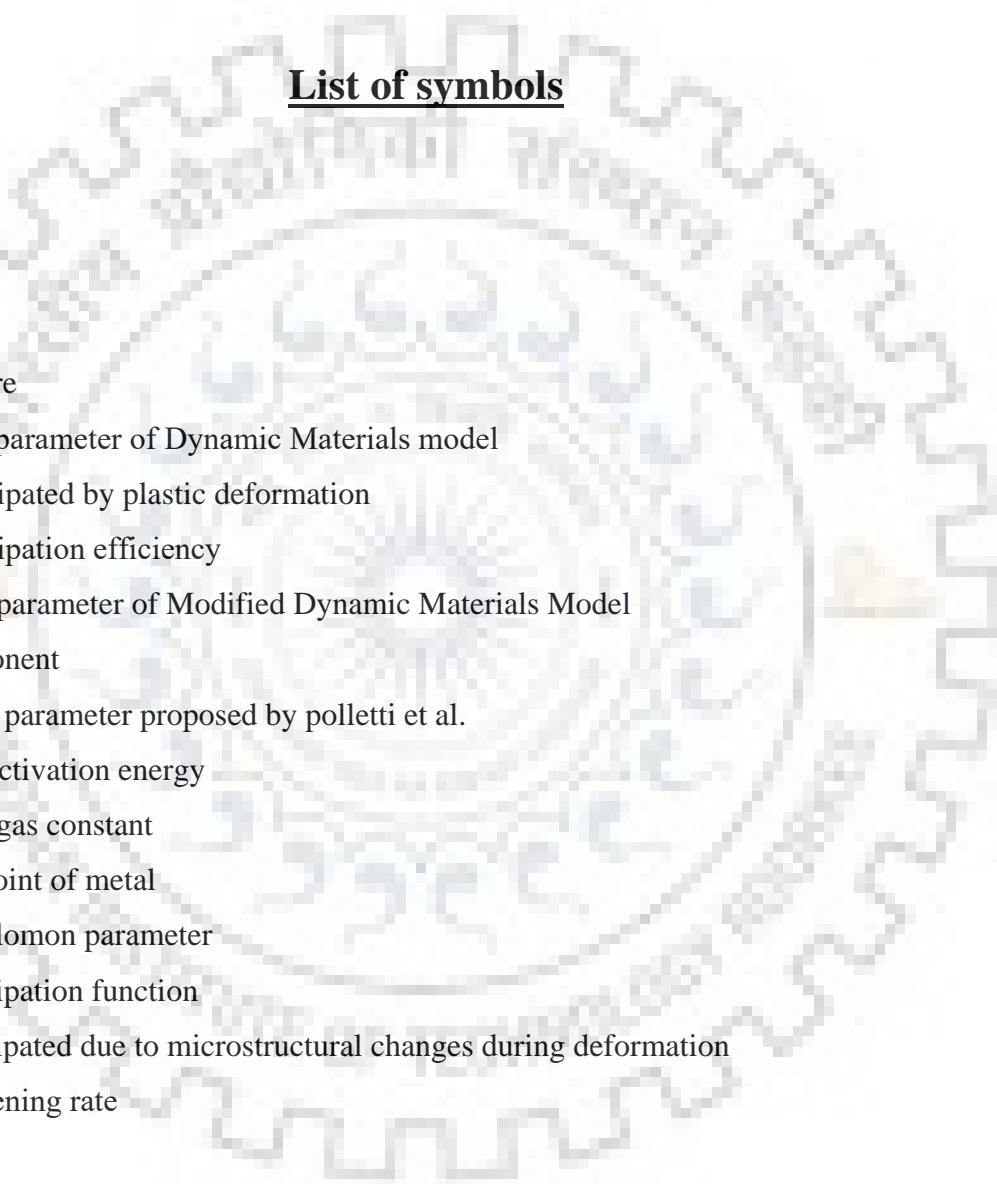
List of figures

Fig. 3.1	sample prepared for dilatometry test	12
Fig. 3.2	Sample prepared for compression test.....	13
Fig. 3.3	Schematic diagram showing compression test plan	14
Fig. 3.4	External view of thermomechanical simulator Gleeble® 3800	15
Fig. 3.5	Schematic diagram of compression testing chamber	15
Fig. 3.6	Leica DMI 5000 light optical microscope	16
Fig. 3.7	EVO18 Ziess scanning electron microscope (SEM)	17
Fig. 4.1	Behaviour of viscoplastic material with strain sensitivity.....	19
Fig. 4.2	Schematic representation of of stress-strain rate curve showing the G and J part	19
Fig. 5.1	Microstructure of as-received high carbon low alloy steel showing spheroidised cementite in ferrite matrix.....	22
Fig. 5.2	Result of Dilatometry test showing critical temperatures	23
Fig. 5.3	True Stress-Strain Curves of specimens deformed at temperature range of 850-1100°C at (a) 0.01s ⁻¹ (b) 0.1 s ⁻¹	24

Fig. 5.4 True Stress Strain Curve for specimens deformed at 850-1100 °C at (a) 1 s ⁻¹ (b) 10 s ⁻¹	25
Fig. 5.5 Curves corrected for Adiabatic temperature rise with experimental true stress-strain curves of specimens deformed at temperature range of 850-1100°C at (a) 0.01s ⁻¹ (b) 0.1 s ⁻¹	27
Fig. 5.6 Curves corrected for Adiabatic temperature rise with experimental True Stress-Strain Curves of specimens deformed at temperature range of 850-1100°C at (a) 1s ⁻¹ (b) 10 s ⁻¹	28
Fig. 5.7 Relationship between true strain and (a) n (b) n' (c) α (d) β (e) lnA using five degree polynomial fit.....	31
Fig. 5.8 Variation of activation energy versus strain (a) Q _p (b) Q _{exp} (c) Q _{sinh} using five degree polynomial fit.....	32
Fig. 5.9 Relationship between ln(Z) vs ln(sinh(ασ)) at true strain of 0.6	32
Fig. 5.10 Plots showing predicted flow stress with experimental True Stress-Strain Curves of specimens deformed at temperature range of 850-1100°C at (a) 0.01s ⁻¹ (b) 0.1 s ⁻¹	33
Fig. 5.11 Plots showing predicted flow stress with experimental True Stress-Strain Curves of specimens deformed at temperature range of 850-1100°C at (a) 1s ⁻¹ (b) 10 s ⁻¹	34
Fig. 5.12 Processing maps developed as a function of strain rate and deformation temperature (°C) for strain of 0.3 (left) and 0.6 (right). (a) and (b) strain sensitivity maps, (c) and (d) DMM based maps.....	36
Fig. 5.13 Processing maps developed and plotted on scale of strain rate and deformation temperature(°C) for strain of 0.3 (left) and 0.6 (right). (a) and (b) modified DMM based maps, (c) and (d) modified DMM efficiency and instability parameter of Polletti[23]	37
Fig. 5.14 Schematic diagram showing the area of interest for microstructural study of deformed cut specimen.....	38
Fig. 5.15 optical micrographs of high carbon low alloy steel after deforming at 900°C showing ferrite(bright) and martensite (dark).A crack can be observed in micrograph of sample deformed at 10 s ⁻¹	39

Fig. 5.16 Optical micrographs of high carbon low alloy steel after deforming at 1100°C.....	40
Fig. 5.17 SEM micrographs of steel specimen after hot compression showing various defects ..	41
Fig. 6.1 Artificial Neural Network Model	43
Fig. 6.2 Comparison between the experimental and predicted flow stress (MPa) by ANN model at different strain rates and temperatures (a) 0.01s ⁻¹ (b) 0.1 s ⁻¹	44
Fig. 6.3 Comparison between the experimental and predicted flow stress by ANN model at different strain rates and temperatures (a) 1s ⁻¹ (b) 10 s ⁻¹	45
Fig. 6.4 Comparison between experimental flow stresses and calculated flow stresses: (a) Training data points (b) Validation data points (c) Test data points (d) All data points	46
Fig. 6.5 Comparison of flow stress (MPa) predicted by (a) Constitutive modelling (b) ANN Modelling.....	47
Fig. 7.1 Strain hardening rate (θ) versus true stress at (a) 0.01 s ⁻¹ (b) 0.1 s ⁻¹ (c) 1 s ⁻¹	49
Fig. 7.2 Strain hardening versus strain at (a) 900°C (b) 1000°C (c) 1100°C	50
Fig. 7.3 Curves of $d\theta/d\sigma$ versus σ at strain rate of (a) 0.01 s ⁻¹ (b) 0.1 s ⁻¹ (c) 1 s ⁻¹	51
Fig. 7.4 Coincidence of predicted steady state strain with work hardening rate and with the model used for calculation of recrystallized fraction. showing nearly 98% DRX for 0.01 s ⁻¹	52
Fig. 7.5 Correlation between (a) critical stress and peak stress (b) critical strain and peak strain	53

List of symbols



σ	Flow stress
ε	True strain
$\dot{\varepsilon}$	Strain rate
T	Temperature
ξ	Instability parameter of Dynamic Materials model
G	Power dissipated by plastic deformation
η	power dissipation efficiency
κ	Instability parameter of Modified Dynamic Materials Model
n	Stress exponent
κ_j	Instability parameter proposed by polletti et al.
Q	Apparent activation energy
R	Universal gas constant
T_m	Melting point of metal
Z	Zener-Hollomon parameter
D	power dissipation function
J	Power dissipated due to microstructural changes during deformation
θ	Strain hardening rate

CHAPTER 1 Introduction

Even with the availability of polymeric, ceramic and composite materials with improved properties for many years now still the use and importance of steels in structural applications continues to lead. Applications such as military equipments, ship building, nuclear power plant applications, aerospace, automobiles etc. still demand huge tonnage of special steel. There is always a demand to reduce the cost of raw material and the processing. Rolling, forging and extrusion are the main bulk deformation processes that are generally performed at temperature greater than two thirds of melting point of metal. Earlier the trial and error techniques were in use to optimise the material forming processes. But the main disadvantage is that the trial-and-error method is unsuitable for small batch production or for new materials developed and becomes very costly and time consuming. Hot deformation of the metals generally involves large strains and high speed of deformations. Large deformation in a single step is permitted because of high temperature that suppresses the cracks and final product is obtained in minimum number of steps. Thermomechanical processing includes the heating and deformation operations under controlled process parameters like strain rate, strain and temperature and also post deformation cooling rate. It is a combined approach of mechanical processing and physical metallurgy to develop a unified approach towards process development. During thermochemical processing desired phase transformations, restoration phenomena like dynamic recrystallization, dynamic recovery and homogenisation with controlled parameters can be obtained which leads to the desirable properties of material. Hence, Thermomechanical processing is the method to control the hot deformation processes and parameters which results in improvement of mechanical properties of materials.

Hot working generally deals with controlling the various parameters such as heating rate, holding temperature, deformation temperature, strain applied, strain rate and post deformation cooling rate. These factors decide the final microstructure and properties of the steel. Generally, thermomechanical processing is focused on the metallurgical aspects to obtain the microstructure with desired mechanical properties. Various defects are generated during hot deformation such as fractures and flow localizations which limits the workability of steels. During hot

deformation, energy from the source is given to the tool. Tools store that energy by their elastic deformation and then energy is transferred to the specimen via an interface. Workpiece undergoes plastic deformation and act as a dissipater of energy, but the whole system is dynamic so the energy transactions are considered in terms of power. So the response of the system also depends upon the rate of energy transfer. In case of hot deformation we can consider it as the strain rate.

1.1 Hot workability and processing maps

Strain rate is not the only parameter which affects the workability of the material. Dieter[1] has presented all the parameters influencing the workability. These parameters are (a) materials chemistry, the initial microstructure, processing history including thermomechanical treatments, (b) the applied temperature, strain rate and strain, (c) applied state of stress and (d) the state of stress existing in the deformation zone. The term hot workability can be understood in terms of how a material is deformed at high temperature in the plastic range of deformation without the incidence of any localization of flow. Parameters like strain, strain rate and temperature are necessary to explain the flow behaviour of material and to formulate the mathematical model for the deformation behaviour. The values of these parameters can be used to create deformation maps separating the safe region from the instable region of hot working parameters. Hot workability can be optimized using different approaches like evaluation of kinetic parameters by examination of stress strain curves and by developing the processing maps using different approaches and criterion. Processing maps are created by superimposing two maps i.e. power dissipation efficiency map and instability map on the axis of temperature and strain rate. Power dissipation maps are formed using dynamic materials model (DMM) of Prasad et al.[2] and Murthy and Rao[3] approach using modified dynamic materials model (DMM).

To know about the phases and microstructure knowledge of transformation temperature of that alloy is necessary. Continuous cooling compression test or dilatometry tests are used to know the transformation temperatures. These transformation temperatures help us in determining the deformation temperature and its range.

By working in the safe workable region, materials strength increases with reduction in its grain size according to the Hall-Petch equation. High strength to weight ratio is always preferable in the steel parts used in automobiles industry. It is well known fact that ferritic grain refinement increases the yield strength of steel. Dynamic recrystallization of ferrite, deformation

and annealing of martensite, deformation induced ferrite transformation [DIFT] are found to be better processing routes for this production of steel.

There are many studies on hot deformation behaviour of plain carbon steel, low carbon microalloyed steel and stainless steel. But the systematic investigation of hot deformation characteristics of high carbon low alloy steel is lacking. Thus, the present work is about the investigation of hot deformation characteristics of high carbon low alloy steel in a manner to find the safe region of processing that is inherent to the material. In this work compression tests at high temperature are carried out on on Gleeble® 3800 thermomechanical simulator in temperature range of 850°C - 1100 °C and strain rates from 0.01 - 10 s⁻¹ up to the total true strain of 0.69. From stress-strain curves obtained parameters like strain rate sensitivity, efficiency of power dissipation, instability parameters are calculated using different instability criteria.

1.2 Artificial Neural Network Modelling

Artificial Neural Network can prove to be a very useful tool in predicting the material behaviour in variable conditions. There is no necessity of any mathematical model to calculate the output rather it learns if there is any pattern in given data in repeated runs and iterations. Then it applies that to new data to predict whole output. Artificial Neural Networks are made up of fundamental units known as nodes similar to the enormous network of neurons found in human a brain.

Artificial Neural Network overcomes the inherent disadvantages of mathematical modelling because it does not consider intrinsic physical mechanisms of deformations rather it has ability to process large random data. So, ANN model can be used to forecast the high temperature flow behaviour of material under known input conditions of working.

1.3 Determination of critical conditions of Dynamic recrystallisation

Dynamic recrystallisation phenomenon is generally verified from the peak observation in the flow curve. However, a material may show some amount of DRX even without showing distinct peak. So, DRX actually begins before the strain corresponding to the peak stress is reached. So, it is very difficult to observe the critical stress from the experimental flow curve which stays smooth before and after critical stress point. A method developed by Ryan and McQueen[4] can be used to find out the onset of Dynamic recrystallisation.

CHAPTER 2 Literature review

2.1 Hot deformation of Steels

Rastegiri et al.[5] deformed the plain carbon eutectoid steel in the temperature range of 620 to 770 °C at a strain rate of 0.01 to 10 s⁻¹ and plotted on temperature strain rate space. They found that dynamic spheroidisation by cementite fragmentation occurs in the range 640 to 720 °C and 0.01-0.1 s⁻¹. Further various processing defects such as flow localisation, lamella sliding, lamella kinking, lamella cracking and prior austenite grain boundary cracking were observed.

Zhang et al.[6] studied the hot compression behaviour of low carbon steel in the temperature range of 650- 1000 °C. No processing maps were developed but the occurrence of microcracks after 70% compression at all the temperatures was found.

Rastegiri et al.[7] also deformed vanadium microalloyed eutectoid steel. It was found that vanadium carbides at grain boundaries strengthened the pearlitic microstructure and reduced the creation of some micro-cracks at high speed deformation.

Ebrahimi et al.[8] performed hot compression test in the temperature range of 850- 1150 °C and in the strain rates of 0.001- 100s⁻¹ to study the hot deformation behaviour of medium carbon low alloy Steel. The processing maps indicated that dynamic precipitation of carbon particles do not affect the rate of dissipation of power. The carbide precipitation also did not lead to any instability in the material. Instability was found at 850 °C and its strain rates of 100 s⁻¹ because of the formation of shear bands.

Yang et al.[9] studied the hot deformation behaviour of low carbon bainitic steel in the temperature range 800-1100 °C and at a strain rate range of 0.001 to 0.1s⁻¹ and found a correlation coefficient of 0.982 between experimental and predicted stress values. The optimum working conditions were found to be 930 to 980°C and 0.001 to 0.014 s⁻¹ with a fully dynamically recrystallized structure with fine-grains.

Zhang et al.[10] studied the constitutive modelling of processing maps for hot deformation of medium carbon Cr-Ni-Mo alloyed Steel at temperature range 900- 1150 °C and at a strain rate range of 0.002-5s⁻¹. Constitutive equations were developed by using work hardening curve for WH-DRX and Avrami equation for the DRX. Also the optimum hot working conditions were defined for 34 Cr-Ni-Mo Steel.

Zhang et al.[11] studied the hot compression behaviour of coiled tubing steel at temperature range of 850- 1100°C and in the strain rate range of 0.001- 5 s⁻¹ and modelled the behaviour by hyperbolic sine constitutive equation. The optimum hot working conditions were found to be at 1015 and 0.01 s⁻¹.

Rajput et al.[12] performed the hot compression test on AISI1010 steel in the temperature range of 750- 1050 °C and strain rates range of 0.01- 20 s⁻¹. Change in Zener-Hollomon parameter (Z) is measured along with the processing maps in the strain rate-temperature space. It was found that lower values of Z promoted restoration processes such as dynamic recrystallization and recovery.

Rajput et al.[13] also studied The hot deformation behaviour of AISI1016 steel in temperature range 750-1050 °C and strain rate of 0.01-80s-1 with total strain of 0.7. Apparent activation energy and stress exponent were also found by hyperbolic sine type of constitutive equation which indicated the plastic deformation mechanism of dislocation glide and climb.

Babu et al.[14] studied the hot deformation behaviour of phosphorus modified super austenitic stainless steel in temperature range of 1173-1423 K at strain rate range of 0.001-10 s⁻¹. They found the optimum processing window in 1300-1350 K and 0.01-0.1 s⁻¹. Although the region of 1300-1350 K and 0.01-0.1 s⁻¹ was marked unstable, still significant DRX and grain refinement occurred in that region.

Ma et al.[15] studied the effect of rare earth alloying on hot workability of duplex stainless steel. They deformed steel in 1223-1473 K and strain rates of 0.01-10 s⁻¹. It was found that Rare earth alloying narrows the hot deformation space and produces the yield point like phenomenon in the flow curves and decreased the mismatch in hardness between produce the mismatch in hardness between softer ferrite and harder austenite.

Pu et al.[16] deformed the super austenitic stainless steel S32654 in the temperature range of 950- 1200 °C and strain rate range of 0.001- 10 s⁻¹. Their processing map showed instability region between 1175 °C and strain rate greater than 0.1 s⁻¹.

Wang et al.[17] studied the hot deformation of ultra high strength steel in temperature range of 950-1080°C and strain rate range of 0.01-10 s⁻¹. They observed an interesting finding that K-P criteria may overestimate the unstable region due to the complex interaction of dynamic precipitation (DP) and DRX which lead to significant deviation from flow stress from the assumed dependence on the strain rate.

G Ji et al.[18] did the compression test on Armet100 steel in the temperature range of 800- 1200 °C and at a strain rate range of 0.01-50 s⁻¹. The optimum safe processing space for Aermet1010 steel was found in the temperature range of 1025-1200°C and at the strain rate range of 0.03 to 15 s⁻¹. Moreover three different instable regions were observed in the processing maps.

K Singh et al.[19] investigated hot deformation behaviour through thermo-mechanical simulations for temperatures ranging from 750°C to 1050°C and with strain rates of 0.001 s⁻¹, 0.01 s⁻¹, 0.1 s⁻¹, 0.5 s⁻¹, 1.0 s⁻¹ and 10 s⁻¹. A comparative study was also carried out between constitutive equation modelling and Artificial Neural Network modelling.

J Yan et al.[20] showed better predictability of flow behaviour by Artificial Neural Network over constitutive equations for Al alloy. A sixteen neuron hidden layer neural network was developed and Mean absolute Error was found to be 1.03% which was better as compared to error by constitutive modelling.

M. Shaban et al.[21] studied the hot deformation behaviour of Nb-Ti microalloyed steel in the temperature range 900-1100°C and strain rate range 0.01-1s⁻¹. The initiation and evolution of dynamic recrystallisation were investigated by analyzing flow curves. A correlation was found between Avrami type of model for calculation of fraction of dynamic recrystallisation and data acquired from experimental curves.

2.2 Hot Deformation

The main advantage of the forming a material at high temperature is that large strains can be achieved with no strain hardening. Hot working is generally defined as deforming the material at temperatures greater than 0.6T_m. Dynamic recrystallization DRX and dynamic recovery DRV are major dynamic restoration processes that occur in metals and alloys. Due to this restoration process the value of stress is low hence deformation of that material becomes easy. With the knowledge of different hot deformation mechanisms, various defects that can occur during deformation can be avoided.

2.3 Deformation mechanisms

Generally there are 6 different mechanisms by which a polycrystalline material can deform. These are

1. Glide of dislocations.
2. Dislocation Creep by climb and cross slip

3. Nabarro-Herring creep
4. Coble creep
5. Twinning
6. Superplastic flow

Each mechanism has its equation which relates stress, strain rate and temperature and structure.

2.4 Strain hardening mechanism

There are some obstacles created in the path of dislocation movement like grain and sub-grain boundaries, solute atoms, second phase particles and other dislocations hinder the movement of dislocations. So on further deformation dislocation density increases and stress required to move those increases. This phenomenon is termed as strain hardening mechanism.

2.5 Softening mechanism

At a certain temperature dislocations achieve adequate mobility to attain interactions and rearrangements into a sub boundaries and sub-grains. So annihilation of the dislocation comes in dynamic equilibrium with their generation by deformation. High stacking fault energy materials such as BCC α -iron, β -Titanium, aluminium etc show more recovery as compared to low stacking fault energy materials. The flow curve during DRV shows a steady state flow stress without showing any peak. In DRX, nucleation occurs due to the high difference in local dislocation density. In DRX, a peak is observed which is followed by a steady state when $\sigma_p > \sigma_s$, where σ_p denotes the peak stress and σ_s denotes the stress for steady state.

2.6 Workability and its evaluation

Workability can be defined as a degree of deformation that can be achieved for a material for a particular metal working process without creating any effects like cracking, fracture, poor surface finish, buckling or the formation of laps etc. Workability can be evaluated by tension, torsion, compression and bend tests. But the compression test is considered as the standard workability test. To avoid buckling of the cylindrical specimen aspect ratio (height to diameter) is limited up to 2.

2.7 Materials modelling in hot deformation

Models of material are expected to predict

1. Evolution of microstructure i.e. materials response.
2. Optimum process parameters
3. Limits to control the process in manufacturing environment.

Prasad and Rao et al.[2] reviewed the models and classified them into four basic types:

1. Kinetic model
2. Atomistic model
3. Dynamic materials model
4. Other models.

2.7.1 Kinetic model

In this model the steady state flow stress is related to temperature and strain rate by Avrami type of equation.

$$\dot{\epsilon} = A\sigma^n \exp\left(\frac{-Q}{RT}\right) \quad (2.1)$$

Where $\dot{\epsilon}$ The strain rate, σ is the steady state flow stress, A is a constant, Q is the activation energy, n is the exponent, T is the temperature, and R is the universal gas constant.

2.7.2 Atomistic models- Raj maps

Raj[22] created atomistic models to calculate the optimum strain rate and temperature that could avoid the microstructural defect during hot deformation. Raj considered parameters for different processes i.e. (1)Formation of voids near hard particles, (2) wedge cracking at the grain boundary triple point, (3) Occurrence of Adiabatic Shear bands, (4) dynamic recrystallization. These maps were basically developed for pure metals and dilute alloys. However the limitation lies in the extension of application to industrial alloys because of lack of data on elementary parameters. This map only gives a broad regime for safe processing and also it becomes impossible to identify the atomistic mechanism that is responsible for deformation and are required for modelling the behaviour.

2.7.3 Dynamic materials model

Dynamic materials model was developed to bring in the constitutive behaviour of materials explicitly into the finite element flow analysis. DMM is actually based of continuum mechanics principle in plastic flow, physical systems modelling, and irreversible thermodynamics. Material is assumed to have following characteristics:

1. **Dissipative:** There is no storage of energy inside the material rather it dissipates the power. Four different types of flow curve that show this type of behaviour of flat type, flow softening after critical strain leading to the steady state, with oscillations where stress becomes damped at large strains and continuous flow softening curve.
2. **Dynamic:** The response of material is mainly influenced by the strain rate and temperature which makes the response dynamic.
3. **Nonlinear:** The flow stress is assumed to be a non linear function of the input variables like temperature, strain rate and strain.
4. **Away from equilibrium:** As strain is not applied in infinitesimally small steps the process of deformation is always away from equilibrium.
5. **Irreversible:** Changes that occur in microstructure during the plastic flow at high temperature are irreversible in nature.

2.7.4 Other models

Other models like activation energy maps, polar reciprocity model also exist. The limitations of these models when compared to DMM these models do not propose any criterion to predict instabilities.

2.8 Research gap

The following research gaps are noticed after critical review of the literature.

1. Studies on hot compression behaviour of plain carbon, microalloyed steels, and low alloy steel exist but no study exists on high carbon low alloy steel especially in high strain rates and high temperatures.
2. Studies on hot deformation in which wide range of processing parameters are used are lacking.
3. The relation of Zener Hollomon parameter Z to the processing maps and flow curves for high carbon low alloy steel has not been studied yet.
4. Study on prediction of flow stress by constitutive modelling for high carbon low alloy steel does not exist.
5. Processing maps for high carbon and low alloy steel has not been developed and analysed.
6. No comparison is available between constitutive modelling and Artificial Neural Network modelling.
7. Critical conditions for Dynamic recrystallisation have not been found for high carbon low alloy steel.

2.9 Problem formulation

Knowledge about the workability of the high carbon low alloy steel is needed by conducting uniaxial isothermal compression experiments. Optimum processing conditions in terms of temperature and strain rate will be determined using flow curves, constitutive equations, dynamic materials model (DMM), modified DMM with various instability parameters available in literature. Specific objectives of this research are as follows:

1. To establish the hot deformation behaviour and study the microstructural evolution of the selected material over wide range of deformation temperature and strain rate.
2. To plot the processing map using DMM and modified DMM with different instability parameters as given by Prasad et al.[2], Murti et al.[3], poletti et al.[23] etc.
3. To develop constitutive equations and finding the correlation between theoretical and estimated values.
4. To identify the deformation mechanism based on activation energy estimates
5. To determine the safe and unsafe working region based on processing maps and verify the same by microstructural study
6. To relate Zener Hollomon parameter with the flow curves and microstructural evolution.
7. To compare modelling between constitutive equations based mathematical models and Artificial Neural Network (ANN) model.
8. To calculate critical conditions for Dynamic Recrystallisation(DRX) in terms of critical strain and critical stress.
9. To calculate the fraction of dynamic recrystallisation using Avrami type of model.

CHAPTER 3 Experimental Methodology

The experimental work involves series of hot compression test of samples at elevated temperatures at different strain rates. The work is described in following steps:

3.1 Procurement of the material

High carbon low alloy steel in the form of cylindrical rod of diameter 25 mm and length 100 mm was procured from open market. Chemical composition of the material as determined by Thermo-Jarell Ash Spark emission spectroscope are given in the Table 3.1 Chemical composition of as received steel (wt%) Table 3.1:

Table 3.1 Chemical composition of as received steel (wt%)

C	Si	Mn	Cr	Ni	Mo	S	P
0.6	0.25	0.37	1.16	0.15	0.15	0.012	0.01

3.2 Sample preparation

Specimens are prepared on lathe machine by cutting and turning operation from the steel rods procured. The dimensions of the compression test specimen are 10 mm diameter and 15 mm length as shown in Fig. 3.2. To avoid buckling and promote homogeneous deformation the aspect ratio is kept 1.5. The dimensions of the specimen for dilatometry test are 10 mm diameter and 50 mm length as shown in Fig. 3.1.

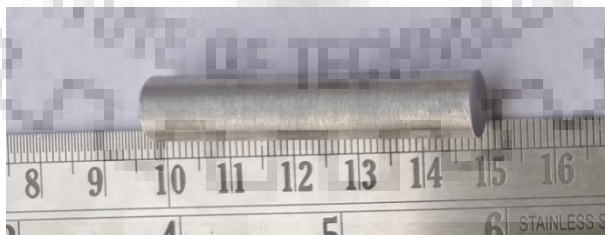


Fig. 3.1 sample prepared for dilatometry test

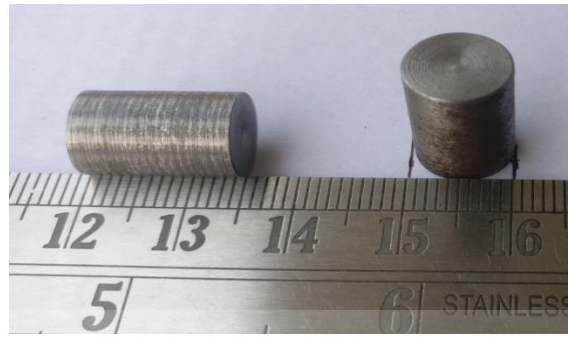


Fig. 3.2 Sample prepared for compression test

3.3 Dilatometry test

Dilatometry test was conducted to define the phase field for the steel. The selection of the deformation temperature will be based on the results of dilatometry test. The CCT dilatometer with LVDT was used in thermomechanical simulator Gleeble[®] 3800. A K-type thermocouple was spot welded at the centre of specimen to record the actual temperature during deformation. For the measurement of temperature specimen is heated at 5 °C/s to the austenitizing temperature. A_{c1} and A_{c3} temperatures were measured. A_{r3} and A_{r1} temperatures were measured during cooling of steel at 1 °C/s. Phase transformation in the steel was detected by accurately measuring the small changes in the diameter of the specimen during the phase transformation. A graph showing the length vs the temperature is produced which shows all critical temperature.

3.4 Uniaxial compression test

The most common and simplest test to determine the workability is uniaxial compression test. These tests were performed on Gleeble[®] 3800 thermomechanical simulator. A schematic showing the compression test parameters is shown in Fig. 3.3 Schematic diagram showing compression test plan. All specimens were heated up to austenitizing temperature with the heating rate of 5 °C/s and soaked for 2 minutes then those were cooled at 1 °C/s to the test temperature as determined by the dilatometry test in the increments of 50 °C. At each temperature the specimens were deformed at the constant strain rates of 0.01, 0.1, 1, 10 s⁻¹. The total targeted true strain was 0.69 which corresponds to 50% deformation. Finally, all the specimens were quenched to freeze the microstructure.

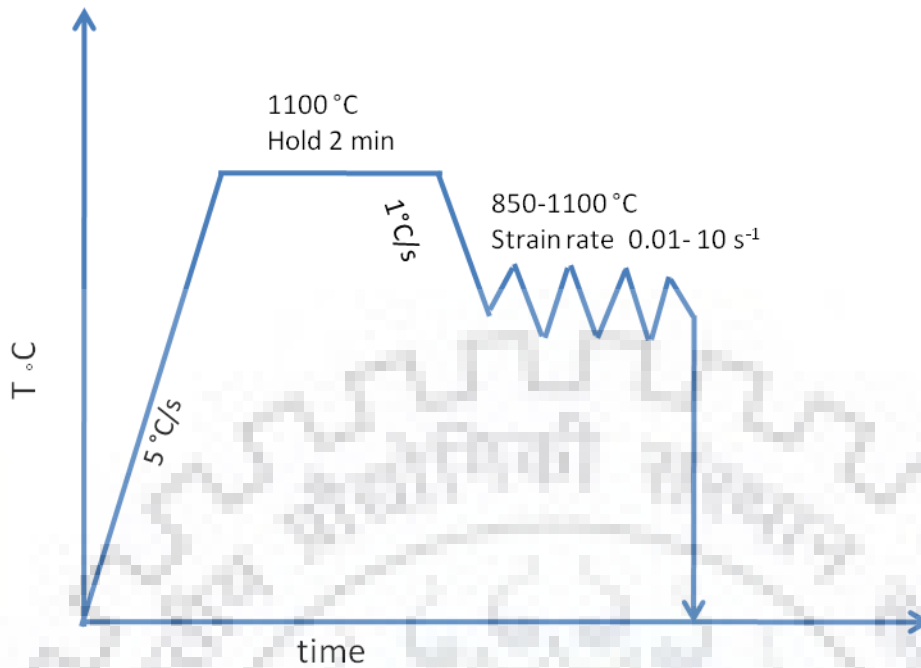


Fig. 3.3 Schematic diagram showing compression test plan

3.5 Gleeble® 3800 Thermo-mechanical simulator

Thermo-mechanical simulator is a testing machine which can simulate the high temperature tests with high strain rate and helps to study the high temperature behaviour of metals and alloys. The external view of Gleeble® 3800 Thermo-mechanical simulator is shown in Fig. 3.4. It mainly comprises of (a) Main control unit (b) The testing unit (c) The hydraulic power unit (d) the vacuum pump unit. External view of Simulator is shown in Fig. 3.4. It is a closed loop feedback system unit which regulates the temperature of specimen by a K-type thermocouple welded at centre of the specimen. Specimen is heated by resistive heating by AC current. Specimen dissipates the heat in the form radiation and conduction from the ends, which are in contact with water cooled jaws. The actuator generates the force and displacement which is measured by the load cell and LVDT respectively. There is a calibration between actuator and load cell. Load cell provides an output voltage proportional to the output force. The LVDT is attached to the base actuator and movable core is positioned by the piston of the actuator. Thus, stroke which is a closed loop mechanical displacement control system gives the constant strain rate deformation during the compression.



Fig. 3.4 External view of thermomechanical simulator Gleeble® 3800

The test specimen is placed between fixed and movable jaw. The movable jaw is operated by a hydraulic-pneumatic system. The schematic of compression testing chamber is shown in Fig. 3.5. The software QuickSim® is used for creating programming for the tests. Data acquisition rate is controllable by programming so 500-1000 data points are acquired for each test.

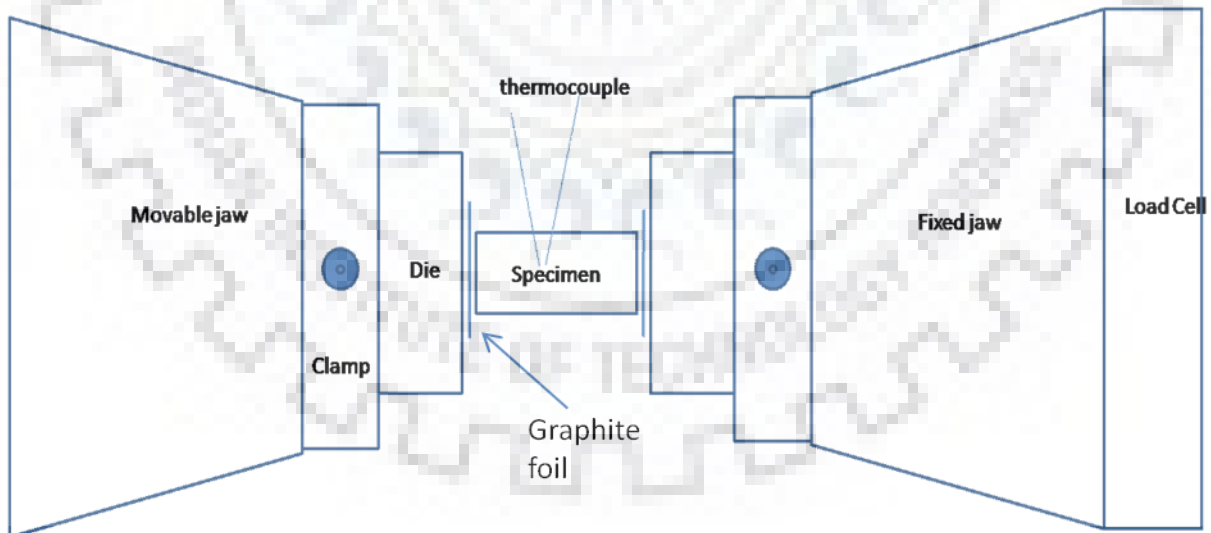


Fig. 3.5 Schematic diagram of compression testing chamber

3.6 Microstructural characterization

Optical microscopy was used to characterize the as received sample. The following steps were taken for the optical microscope (Fig. 3.6)

1. **Sectioning of the sample:** The sample was cut along the section using high speed Diamond cutter to observe the microstructure at the centre.
2. **Grinding:** To prepare the specimen flat and also to remove the strained surface formed during the sectioning process grinding is done on p120 grit polishing papers.
3. **Paper polishing:** then the specimen is polished using p800, p1500, p2000 polishing papers. The specimen was rotated through 90 degree after each polishing step on papers.
4. **Cloth polishing:** the specimen was cloth polished using Alumina grade 1 of size $0.014\mu\text{m}$ on the fine velvet cloth until the all paper scratches were gone.
5. **Cleaning and drying:** sample was cleaned with running cold water and was dried with help of a hot air blower.
6. **Etching** of the prepared specimen was done using 2% Nital solution to reveal the microstructure.

Similar steps were followed for the microstructure characterization of deformed samples.



Fig. 3.6 Leica DMI 5000 light optical microscope

SEM

A EVO18 Ziess scanning electron microscope (SEM) shown in Fig. 3.7 equipped with the LaB₆ filament was used to examine the microstructural features of the hot deformation specimens of each steel.



Fig. 3.7 EVO18 Ziess scanning electron microscope (SEM)

3.7 Measurement of Hardness

Micro hardness test of the specimen is measured by Vickers hardness test using FIE-VM50PC Vickers hardness tester by employing 10 kg load with dwelling time of 10s. Vicker'sTM software is used to measure the diagonals of the impression made and to calculate the hardness.

VMH 104 Microhardness tester was used to measure the hardness using 1 kg load. At least 10 such readings were taken.

CHAPTER 4 Theory and analysis

4.1 Processing maps

Processing maps are plotted on the axes of strain rate and deformation temperature at a constant value of true strain. Ashby[24] gave the concept of processing maps and later on these are improved by Prasad et al.[2] by developing on dynamic materials model. DMM assumes that material does not store energy rather is acts as dissipater. It is known that power P given to the material is expressed as multiplication of stress times the strain rate.

$$P = \sigma \dot{\epsilon} \quad (4.1)$$

Prasad assumed that this power can be split into two parts: G, power dissipated in deforming material plastically and J, power utilised in microstructural changes, as can be seen in schematic representation in Fig. 4.2 .

$$P = G + J = \sigma \dot{\epsilon} = \int_0^{\dot{\epsilon}} \sigma d\dot{\epsilon} = \int_0^{\sigma} \dot{\epsilon} d\sigma \quad (4.2)$$

where σ is the flow stress and $\dot{\epsilon}$ is the strain rate.

$$m = \left(\frac{\partial J}{\partial G} \right)_{T, \epsilon} = \frac{\sigma d\dot{\epsilon}}{\dot{\epsilon} d\sigma} = \left[\frac{\partial \ln \sigma}{\partial \ln \dot{\epsilon}} \right]_{T, \epsilon} \quad (4.3)$$

The significance of strain sensitivity ‘m’ is illustrated by Ziegler[25] for viscoplastic solids as shown in Fig. 4.1 and is described as:

1. $m=0$; it implies that the efficiency of power dissipation is zero and total power is dissipated in increasing the temperature of material
2. $m=1$ indicates superplastic flow of material
3. $0 < m < 1$ indicates stable flow during plastic work.
4. $m > 1$ are called locking solids.

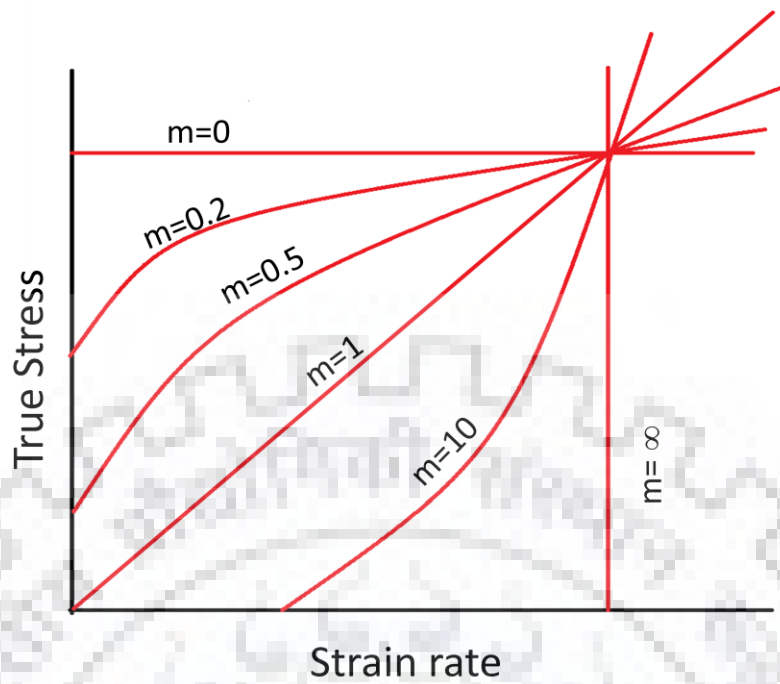


Fig. 4.1 Behaviour of viscoplastic material with strain sensitivity

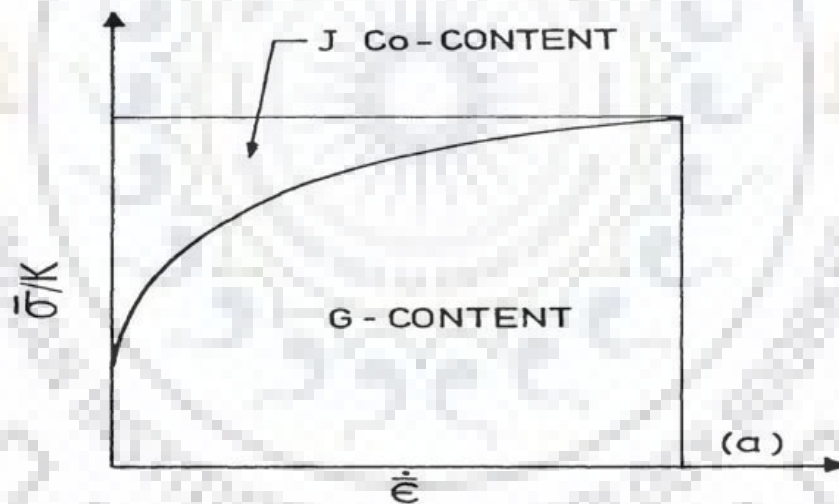


Fig. 4.2 Schematic representation of of stress-strain rate curve showing the G and J part

The power dissipation efficiency η is given by the ratio of J co-content and the maximum J co-content possible.

$$\eta = \frac{J}{J_{max}} = \frac{2J}{P} = \frac{2m}{m+1} \quad (4.4)$$

Murthy and Rao[3] modified the dynamic materials model which is known as modified DMM. Modification was done to avoid the use of strain rate sensitivity in calculation of power dissipation efficiency.

In modified DMM, η is calculated as:

$$\eta = \frac{2(P-G)}{P} \quad (4.5)$$

m is the strain rate sensitivity is defined as:

$$m = \left[\frac{\partial \ln \sigma}{\partial \ln \dot{\epsilon}} \right]_{T, \epsilon} \quad (4.6)$$

Ziegler[25] proposed that the instability occurs when:

$$\frac{\partial D}{\partial \dot{\epsilon}} < \frac{d}{\dot{\epsilon}} \quad (4.7)$$

where D is the power dissipation function.

Montheillet et al.[26] proposed that $D=P$, i.e. total power dissipated. So instability will occur when $m < 0$.

According to DMM, only power dissipated in microstructural changes is taken. So $D=J$.

This results in different instability criteria. These parameters are:

1. As proposed by Prasad et al.[2]

$$\xi(\dot{\epsilon}) = \frac{\partial \ln \frac{m}{m+1}}{\partial \ln \dot{\epsilon}} + 1 < 0 \quad (4.8)$$

2. As proposed by Murthy and Rao[3]

$$\kappa = \frac{2m}{\eta} - 1 < 0 \quad (4.9)$$

3. As proposed by Poletti et al.[23] to remove strain rate sensitivity dependence

$$\kappa_j = \frac{\partial \ln J}{\partial \ln \dot{\epsilon}} - 1 < 0 \quad (4.10)$$

4.2 Basic constitutive equations

Steady state flow stress-strain rate, temperature follows the Kinetic rate equation as:

$$\sigma = K \epsilon^n \dot{\epsilon}^m + Y \quad (4.11)$$

Where n is the strain hardening exponent, m is the strain rate sensitivity and K , Y are coefficients. At room temperature strain hardening exponent is dominant; however at higher temperatures strain rate sensitivity becomes more significant.

4.3 Zener-Holloman parameter

Z temperature takes in to the consideration both temperature and strain rate. Sellars and Tegart[27] proposed a universal constitutive equation:

$$Z = \dot{\epsilon} \exp\left(\frac{Q}{RT}\right) = A[\sinh(\alpha\sigma)]^n \quad (4.12)$$

For low stresses ($c\sigma < 1$) power law expresses the hot deformation behaviour as:

$$Z = \dot{\epsilon} \exp\left(\frac{Q}{RT}\right) = A_p \sigma^{n'} \quad (4.13)$$

While exponential law describes the behaviour for high stresses ($c\sigma > 1.2$),

$$Z = \dot{\epsilon} \exp\left(\frac{Q}{RT}\right) = A_E \exp(\beta\sigma) \quad (4.14)$$

Where Q is the apparent activation energy, R is the gas constant. A_E , A_p , A , c , n' , β and n are material constants.

CHAPTER 5 Results and discussion

5.1 Initial characterization

The optical micrograph of as received sample is shown in the Fig. 5.1

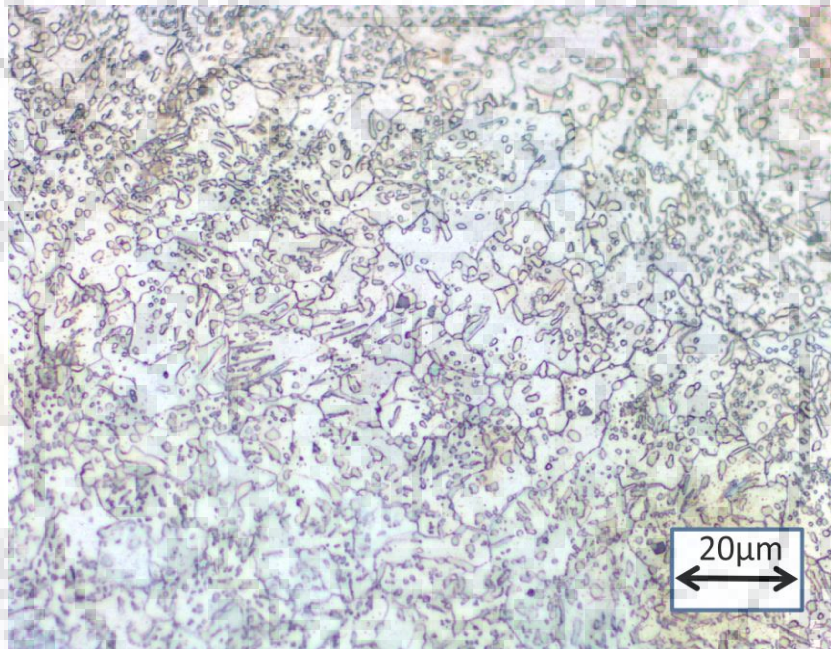


Fig. 5.1 Microstructure of as-received high carbon low alloy steel showing spheroidised cementite in ferrite matrix

Hardness of the as-received specimen is found 200 VHN in Vickers hardness test. Microstructure of the as received sample showed the ferrite matrix in which cementite is present in spheroidized form. This means that the steel is being spheroidised after production. Spheroidization is generally done to improve formability and machinability of high carbon steel. This is the softest and most ductile form of steel. This soft and readily machinable form is produced by the process of heat treatment known as spherodisation. The hardness value is decreased due to the presence of the cementite in spheres as compared to pearlite form.

The critical temperatures were determined by dilatometry test (CCT) on thermo-mechanical simulator using quartz dilatometer. The result of CCT test shows that as the temperature is

increased the dilation in the sample increases upto 786 °C and then decreases upto 845 °C and due to the formation of austenite, further it increased after complete formation of austenite as shown in Fig. 5.2. During cooling the critical temperatures were obtained as 672°C and 640°C.

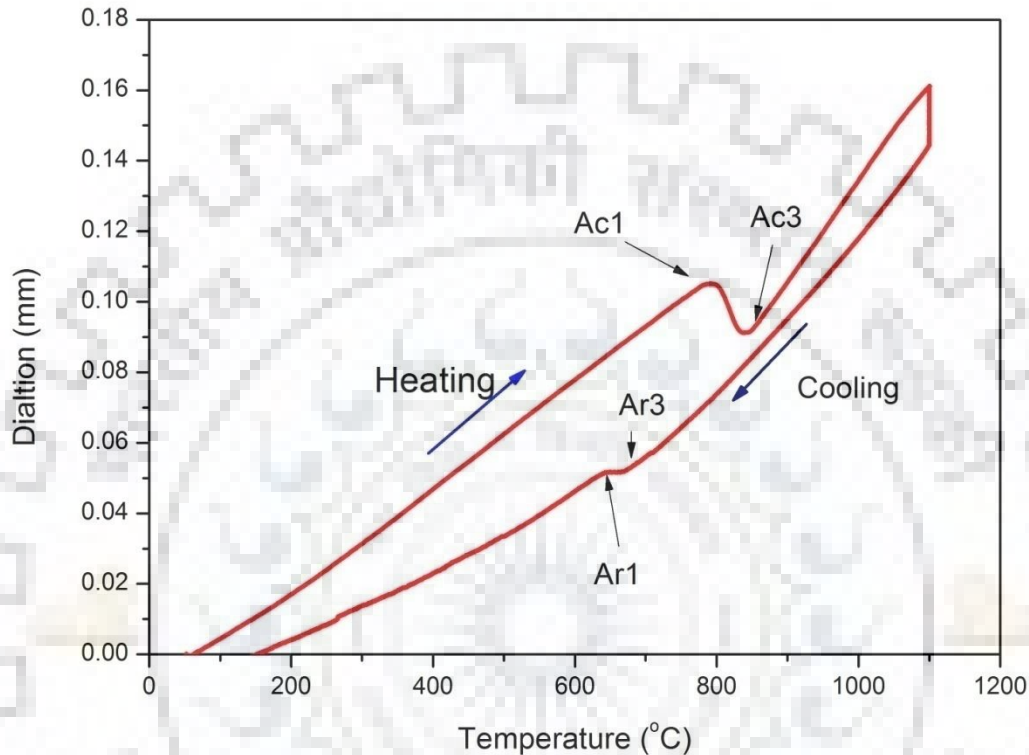


Fig. 5.2 Result of Dilatometry test showing critical temperatures

5.2 True Stress Stress Strain curves

The flow stress values gradually decrease as the temperature increased for a constant strain rate. The flow stress curves show a peak at low strain rate of 0.01 s^{-1} to 1 s^{-1} after Strain hardening. After peak stress softening phenomenon is observed then subsequently showing the steady state. The peak in flow curve shows the phenomenon of Dynamic recrystallisation(DRX). As the deformation temperature is reduced, peak shifts towards lower strain rate. This is because of at lower strain rate or higher temperatures rate of work softening increases in comparison with work hardening rate. The strain hardening is observed due to dislocation generation. Other specimens which were deformed at strain rate of 10 s^{-1} did not show any peak rather it showed strain hardening zone and the steady state zone. The stress strain curves without peak shows the

phenomenon of Dynamic Recovery (DRV). When dislocation generation is balanced by dislocation annihilation (softening) flow curve shows a plateau instead of a peak. The occurrence of DRX and DRV can also be predicted with the help of Zener-Hollomon parameter. When Zener Hollomon Parameter Z is high DRV occurs whereas DRX occurs for low values of Z . Fig. 5.3 and Fig. 5.4 shows that for fixed strain rate the values flow stress decreases as temperature increases.

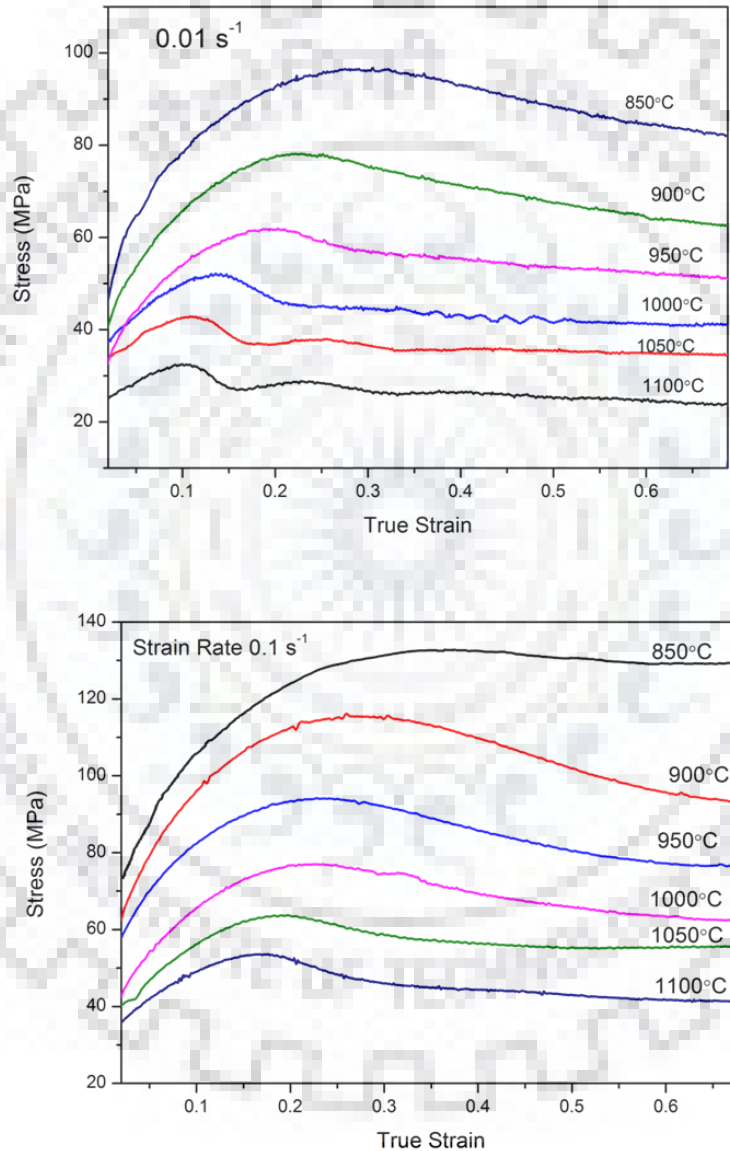


Fig. 5.3 True Stress-Strain Curves of specimens deformed at temperature range of 850-1100°C at (a) 0.01 s^{-1} (b) 0.1 s^{-1}

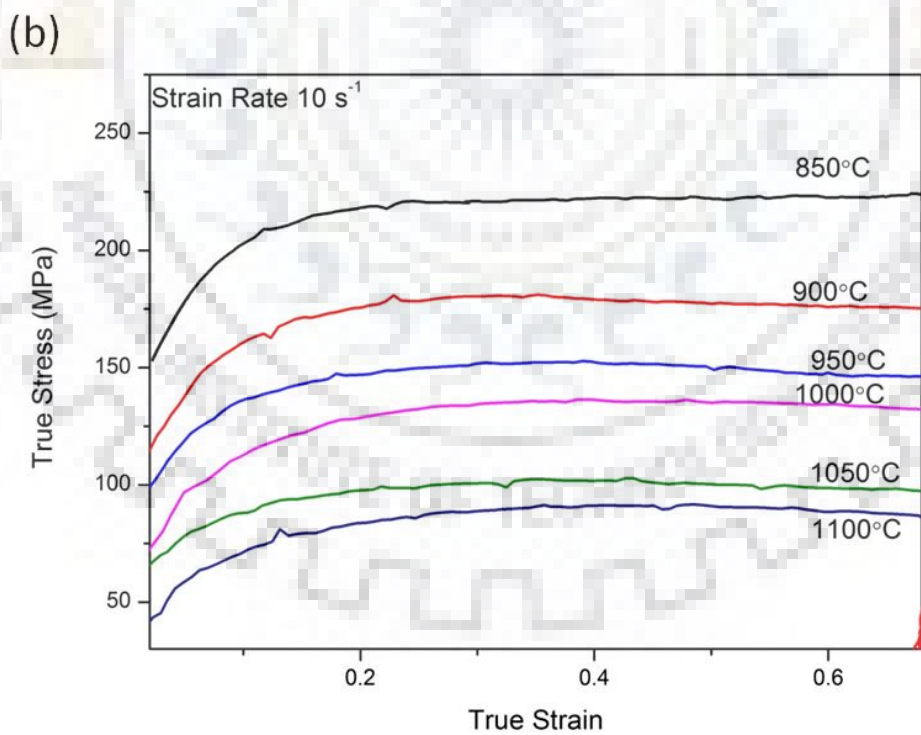
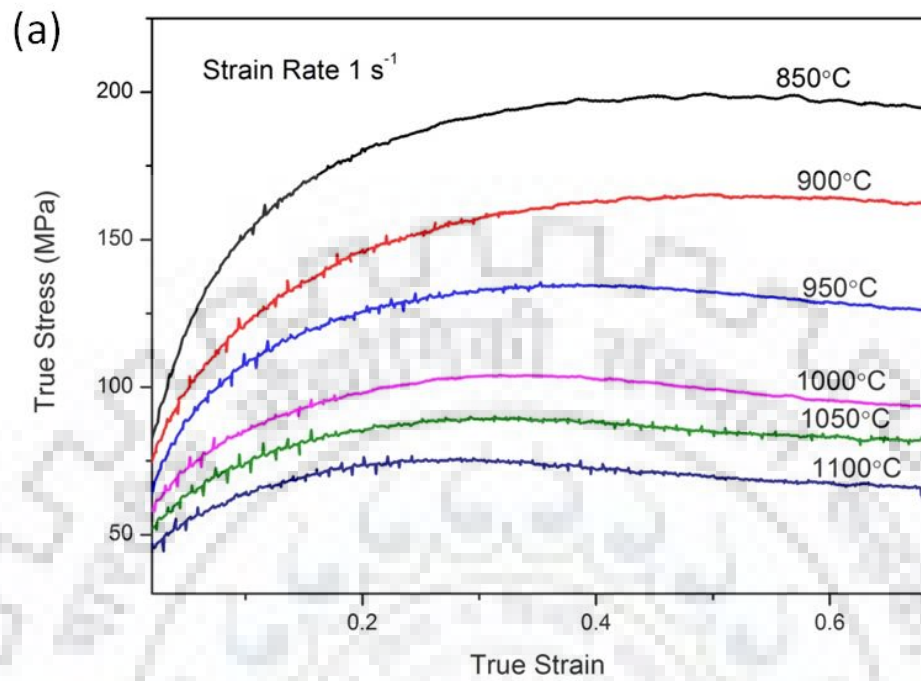


Fig. 5.4 True Stress Strain Curve for specimens deformed at 850-1100 °C at (a) 1 s^{-1} (b) 10 s^{-1}

5.3 Correction for Adiabatic Temperature Rise

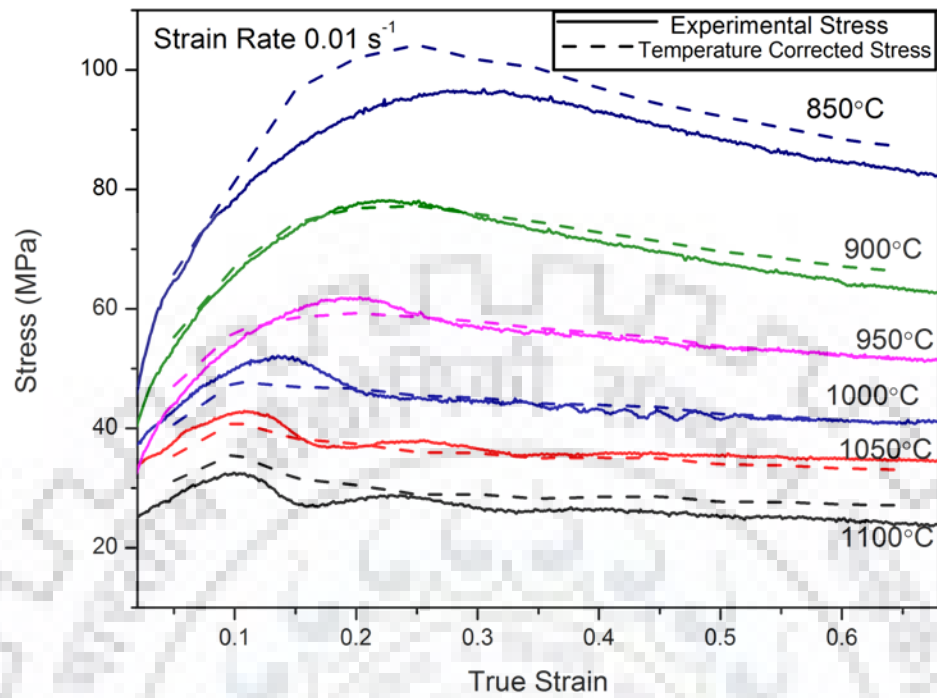
As heat generation is an inevitable phenomenon in plastic deformation, this heat has to be dissipated otherwise it results in an increase of temperature. At higher strain rates, nearly adiabatic conditions are formed, and the heat generation rate is significantly higher than the heat dissipation rate. This results in an adiabatic temperature rise. As the time for deformation is very less, so heat dissipation is insignificant as compared to heat generation, so the temperature rise can be as high as 40°C at a strain rate of 10 s⁻¹ and a temperature of 850 °C. The values of adiabatic temperature rise are summarised in Table 5.1. Maximum temperature rise during hot deformation with different temperatures and strain rates. As the deformation temperature is higher due to this adiabatic heating, so the values of flow stress need to be corrected to get the value at the desired temperature. Adiabatic temperature corrections were made using the linear interpolation method between ln(σ) and 1/T (taking T in Kelvin) at constant strain rate and strain.

Table 5.1 Maximum temperature rise during hot deformation

Temperature	dT at strain rates (s ⁻¹)			
	0.01	0.1	1	10
850	3.34	12.39	15.28	36.78
900	4.6	10.77	18.80	27.30
950	5.4	11.21	14.27	22.04
1000	6.86	3.55	19.16	23.85
1050	7.08	3.72	10.10	18.80
1100	3.21	3.42	11.11	16.80

As shown in Fig. 5.5 and Fig. 5.6, corrected true stress shows a higher value to compensate for the adiabatic temperature rise for all the curves. It can be observed that there is a significant rise in temperature at lower deformation temperatures because a higher amount of energy is required to deform at lower temperatures, which also results in energy conversion to heat.

(a)



(b)

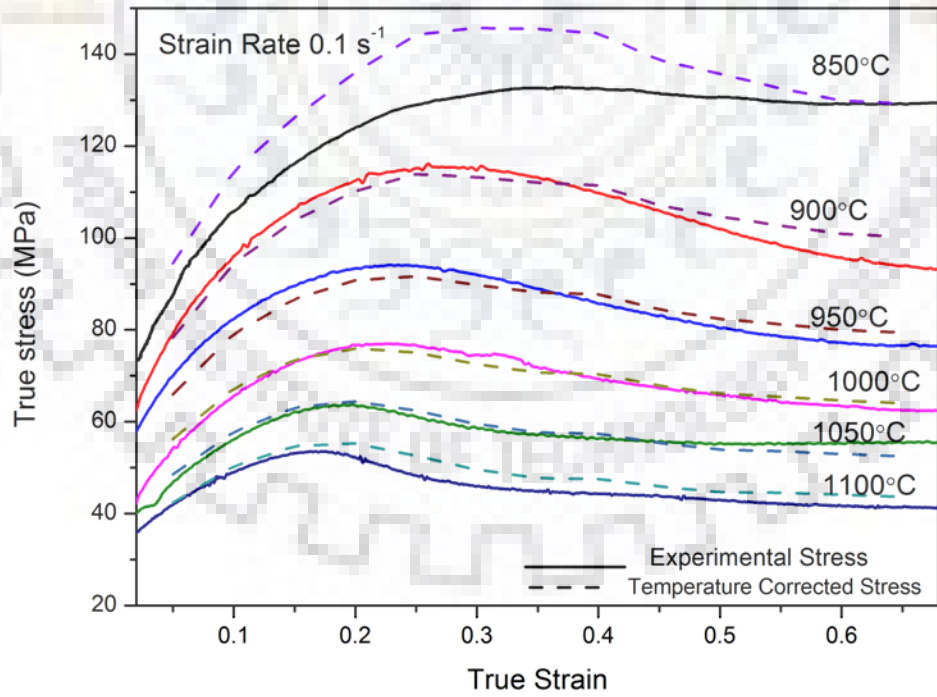


Fig. 5.5 Curves corrected for Adiabatic temperature rise with experimental true stress-strain curves of specimens deformed at temperature range of 850-1100°C at (a) 0.01 s^{-1} (b) 0.1 s^{-1}

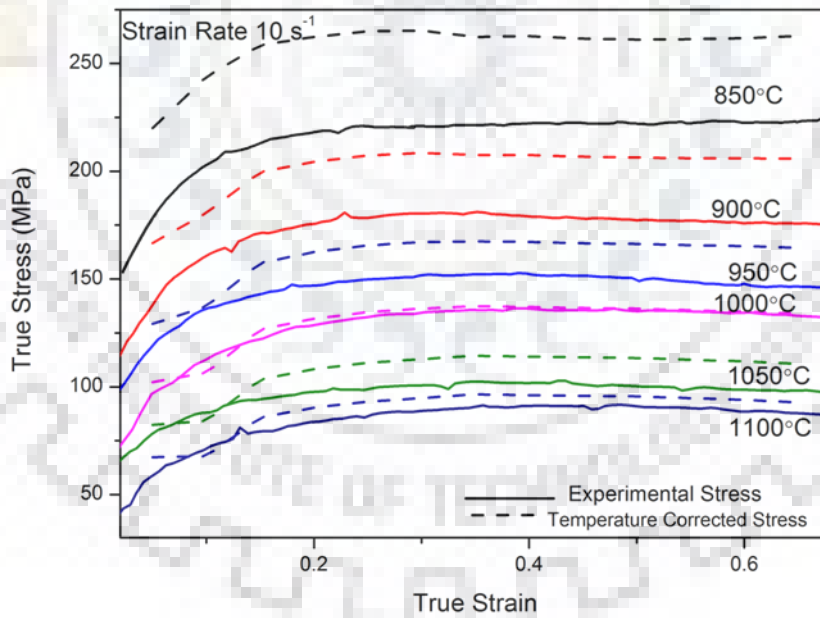
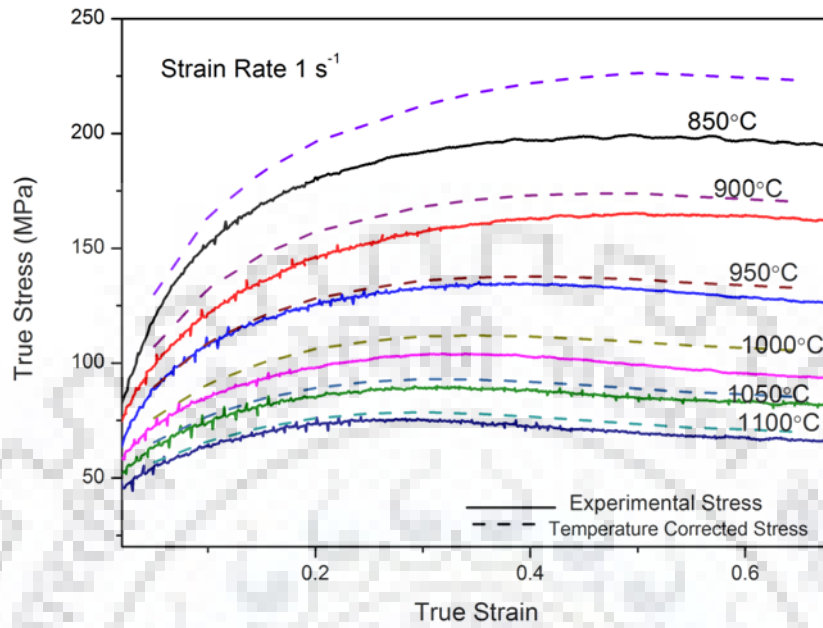


Fig. 5.6 Curves corrected for Adiabatic temperature rise with experimental True Stress-Strain Curves of specimens deformed at temperature range of 850-1100°C at (a) 1 s^{-1} (b) 10 s^{-1}

5.4 Constitutive Equation analysis

Different deformation mechanism can be analysed using constitutive equations. Material constants can be found using the Eq 4.11, 4.12 and 4.13, by taking natural log on both sides,

$$\ln \dot{\epsilon} + \left(\frac{Q}{R}\right) \left(\frac{1}{T}\right) = \ln C + n' \ln \sigma \quad (5.1)$$

$$\ln \dot{\epsilon} + \left(\frac{Q}{R}\right) \left(\frac{1}{T}\right) = \ln B + \beta \sigma \quad (5.2)$$

$$\ln \dot{\epsilon} + \left(\frac{Q}{R}\right) \left(\frac{1}{T}\right) = \ln A + n \ln[\sinh(\alpha \sigma)] \quad (5.3)$$

Partially differentiating Eq 5.1, 5.2 and 5.3 respectively gives the following equations,

$$n' = \left[\frac{\partial \ln \dot{\epsilon}}{\partial \ln \sigma} \right]_T \quad (5.4)$$

$$\beta = \left[\frac{\partial \ln \dot{\epsilon}}{\partial \sigma} \right]_T \quad (5.5)$$

$$n = \left[\frac{\partial \ln \dot{\epsilon}}{\partial \ln \{\sinh(\alpha \sigma)\}} \right]_T \quad (5.6)$$

These expressions represent that the slope of $\ln \dot{\epsilon}$ versus $\ln \sigma$ and the slope of $\ln \dot{\epsilon}$ versus σ is used to obtain the value of n' and β respectively. Flow stress data for true strain of 0.1 to 0.65 is obtained in the steps of 0.05. the value of α is obtained by $\alpha = \beta/n'$. The value of stress exponent (n) can be used to predict the mechanism of dislocation. Among Arrhenius type equations, the sinh type of law gives better estimation between Zener-Hollomon parameter and flow stress. By partially differentiating Eq 5.3 at a constant strain rate, hot deformation Activation Energy can be obtained.

$$Q = Rn \left[\frac{\partial \ln(\sinh(\alpha \sigma))}{\partial \left(\frac{1}{T}\right)} \right]_{\dot{\epsilon}} \quad (5.7)$$

Linear relationship between $\ln(Z)$ with $\ln(\sinh(\alpha \sigma))$ can be obtained by taking logarithm on both sides of equation 4.12 and putting the values of the strain rate, temperatures and for true strain of

0.6, whose intercept yields the value of material constant A as $4.12 * 10^{13}$. So, a universal constitutive relation for this steel is obtained after putting values of all constants.

$$Z = \dot{\epsilon} \exp\left(\frac{345658}{RT}\right) = 4.12 * 10^{13} [\sinh(0.011661 * \sigma)]^{4.09} \quad (5.8)$$

5.5 Prediction of flow Stress

All the material constants (α , β , n' , n , and $\ln A$) were calculated from the constitutive equations for the strain ranging from 0.1 to 0.65 in the steps of 0.05. All the material constants were assumed to be a polynomial function of strain, thus each constant was fitted with a polynomial equation of 5 degree because it gave the best correlation coefficient of fitting. It was observed as the true strain in the material increases the value of all material constant reduces.

$$\beta = B_0 + B_1\epsilon + B_2\epsilon^2 + B_3\epsilon^3 + B_4\epsilon^4 + B_5\epsilon^5 \quad (5.9)$$

$$\alpha = C_0 + C_1\epsilon + C_2\epsilon^2 + C_3\epsilon^3 + C_4\epsilon^4 + C_5\epsilon^5 \quad (5.10)$$

$$n' = D_0 + D_1\epsilon + D_2\epsilon^2 + D_3\epsilon^3 + D_4\epsilon^4 + D_5\epsilon^5 \quad (5.11)$$

$$n = E_0 + E_1\epsilon + E_2\epsilon^2 + E_3\epsilon^3 + E_4\epsilon^4 + E_5\epsilon^5 \quad (5.12)$$

$$Q = F_0 + F_1\epsilon + F_2\epsilon^2 + F_3\epsilon^3 + F_4\epsilon^4 + F_5\epsilon^5 \quad (5.13)$$

$$\ln(A) = G_0 + G_1\epsilon + G_2\epsilon^2 + G_3\epsilon^3 + G_4\epsilon^4 + G_5\epsilon^5 \quad (5.14)$$

$$\sigma = \frac{1}{\alpha} \ln \left\{ \left(\frac{Z}{A} \right)^{\frac{1}{n}} + \left[\left(\frac{Z}{A} \right)^{\frac{2}{n}} + 1 \right] \right\} \quad (5.15)$$

Fig. 5.10 and Fig. 5.11 shows the predicted flow stress with experimental True Stress-Strain Curves of specimens deformed at temperature range of 850-1100°C at strain rate 0.01 to 10 s⁻¹.

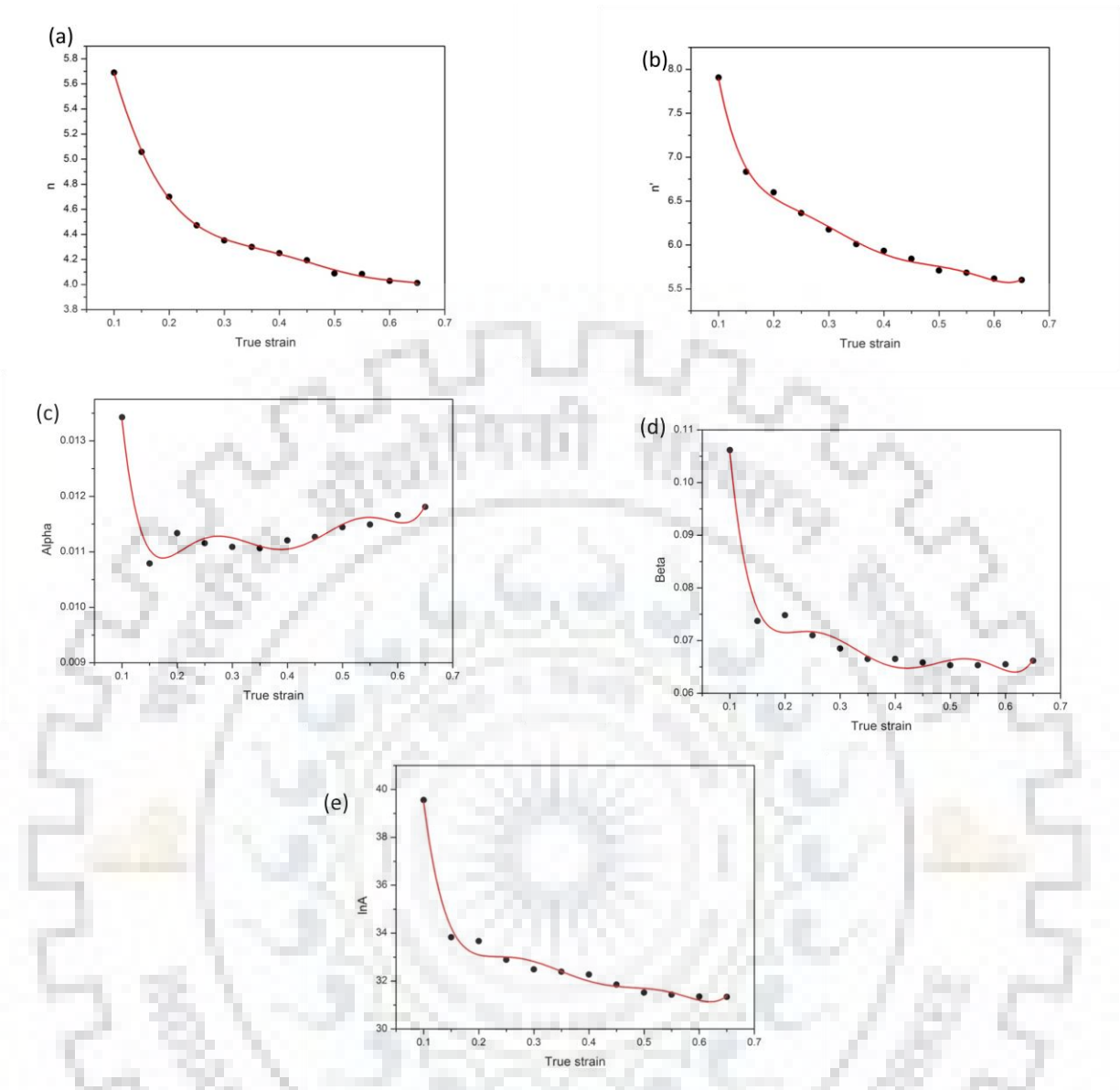


Fig. 5.7 Relationship between true strain and (a) n (b) n' (c) α (d) β (e) $\ln A$ using five degree polynomial fit

The correlation coefficient ($R^2=0.985$) between $\ln(Z)$ vs $\ln(\sinh(\alpha\sigma))$ was found to be maximum in in case of universal equation which shows a better agreement with experimental data as shown in Fig. 5.9.

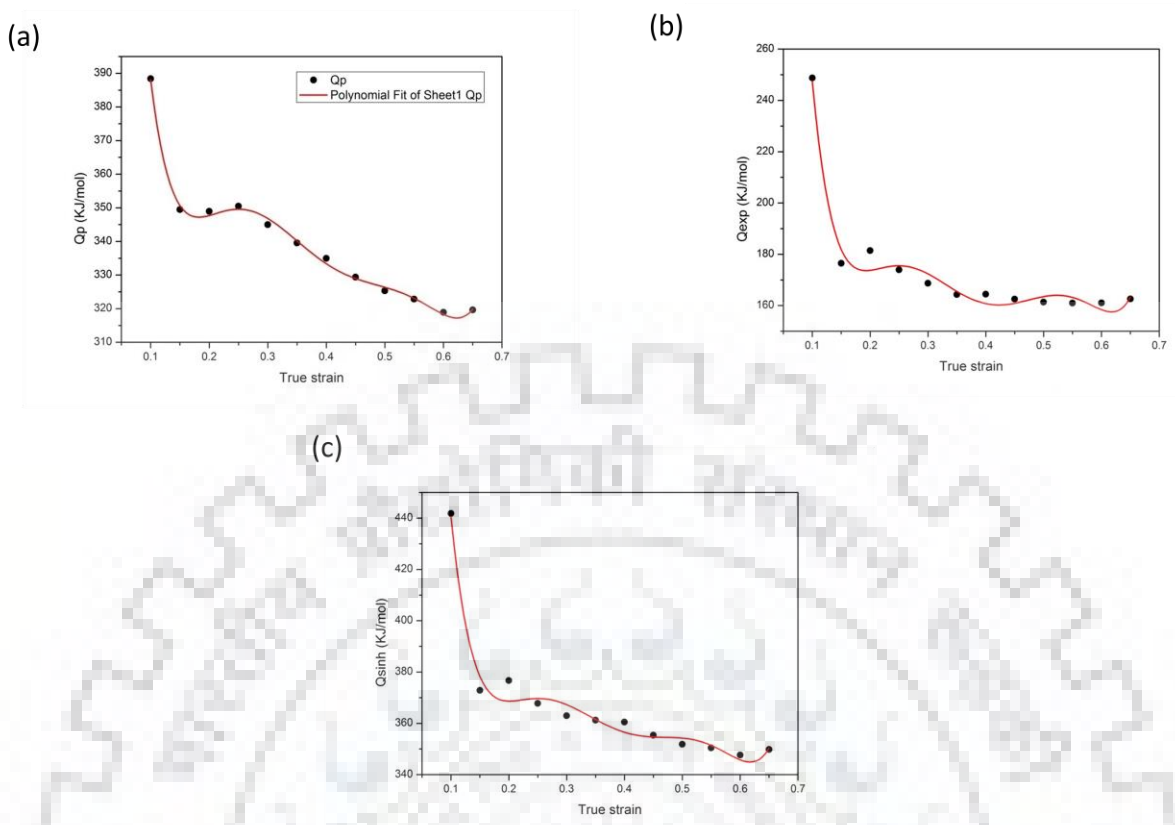


Fig. 5.8 Variation of activation energy versus strain (a) Q_p (b) Q_{exp} (c) Q_{sinh} using five degree polynomial fit

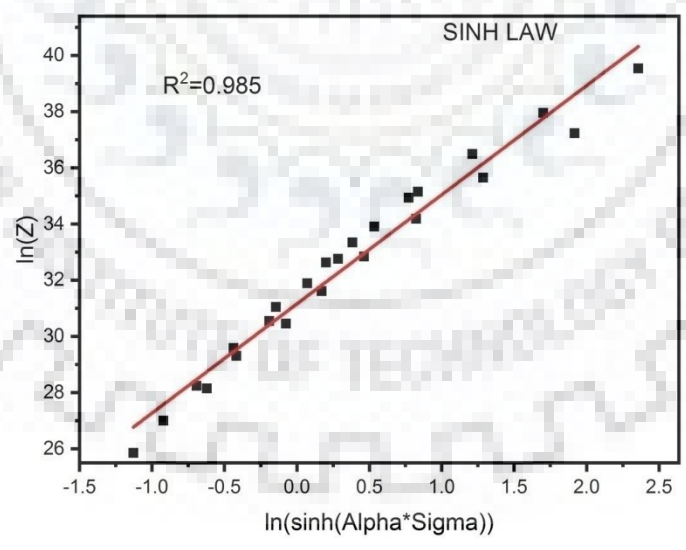


Fig. 5.9 Relationship between $\ln(Z)$ vs $\ln(\sinh(\alpha\sigma))$ at true strain of 0.6

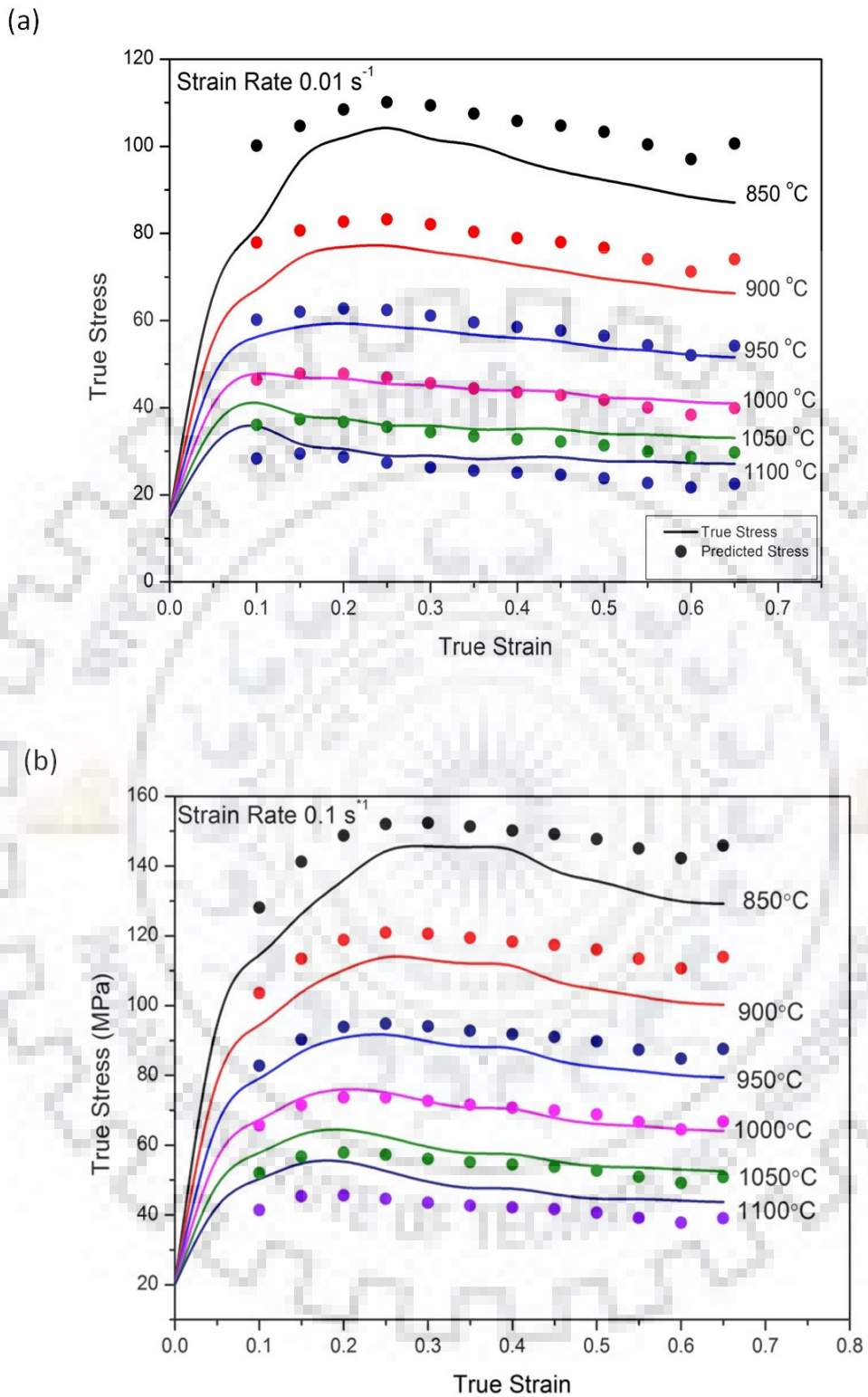


Fig. 5.10 Plots showing predicted flow stress with experimental True Stress-Strain Curves of specimens deformed at temperature range of 850-1100°C at (a) 0.01 s^{-1} (b) 0.1 s^{-1}

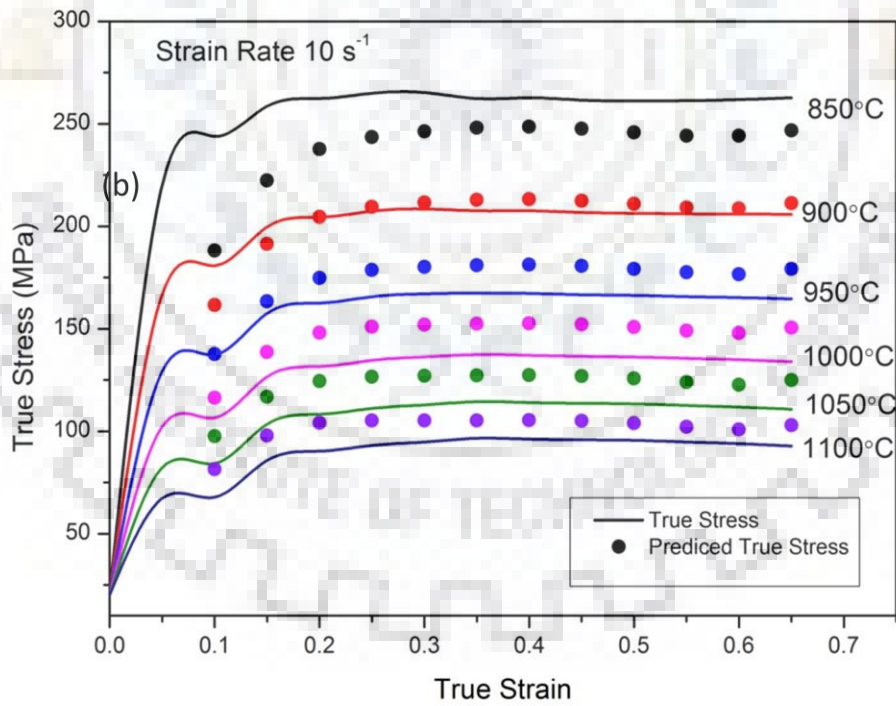
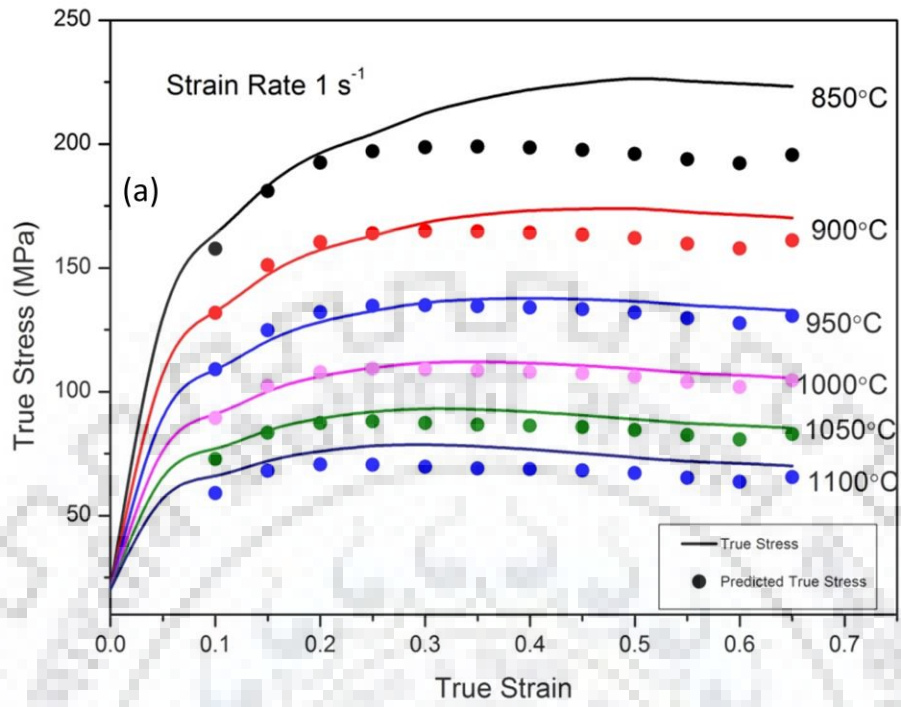


Fig. 5.11 Plots showing predicted flow stress with experimental True Stress-Strain Curves of specimens deformed at temperature range of $850\text{-}1100^\circ\text{C}$ at (a) 1 s^{-1} (b) 10 s^{-1}

5.6 Processing maps

Processing maps were developed strain of 0.3 and 0.6 to avoid the effect of accumulation of strain hardening due to strain hardening. Processing maps of high carbon low alloy steel based on strain rate sensitivity, DMM and modified DMM for true strain of 0.3 and 0.6 are shown in Fig. 5.12 and Fig. 5.13. The strain rate sensitivity (m) calculated using equation 4.6 was plotted for the true strain of 0.3 and 0.6 on axes of temperature and logarithmic scale of strain rate. These maps have positive values of m for the entire range. This means that no instability is predicted by these maps.

5.6.1 Maps based on Dynamic Materials Model (DMM)

Based on DMM power dissipation efficiency (η_{prasad}) and instability parameter (ξ) are plotted on the scale of temperature and logarithm of strain rate and are superimposed on each other to obtain processing maps for 0.3 and 0.6 respectively. It is observed that iso-efficiency lines follow the same trend of strain rate sensitivity contour lines. So broadly two different regions are observed in these DMM based maps:

1. A region with low efficiency in the temperature range of 850-1100°C in the range of strain rate 0.01-0.3 s⁻¹ with maximum efficiency 26%.
2. A peak zone between strain rate range 0.3 s⁻¹ to 10 s⁻¹ and in whole temperature range with minimum efficiency 26%.

Similarly, Fig. 5.13 show the processing maps based on the modified DMM in which iso-efficiency contours of η_{Murty} and instability parameter contour are superimposed at the strain rate of 0.3 and 0.6 respectively. In Fig. 5.13 processing maps based on power dissipation efficiency of Murty and Rao are superimposed with instability parameter of polletti et al. At stain rate of 0.3 and 0.6. It can be inferred that k parameter predicts the larger instability domain as compared to ξ parameter. Whereas the k_j parameter predicted the smallest area of all. The DRX of austenite took place at low strain rates and high temperatures which can also be inferred from the high power dissipation efficiency domain in that region as well as from flow curves. It is observed that values of m and η increased with the increase in temperature for all strain rates. At lower strain rate large values of m and η are observed which shows better workability. Improved workability can also be confirmed by apparent activation energy at lower strain rates.

At high strain rates and lower temperature formation of defects like crack, voids and pores is confirmed by both optical and scanning electron micrographs. These defects are observed due to less time available restoration processes like Dynamic recrystallisation and Dynamic recovery to take place.

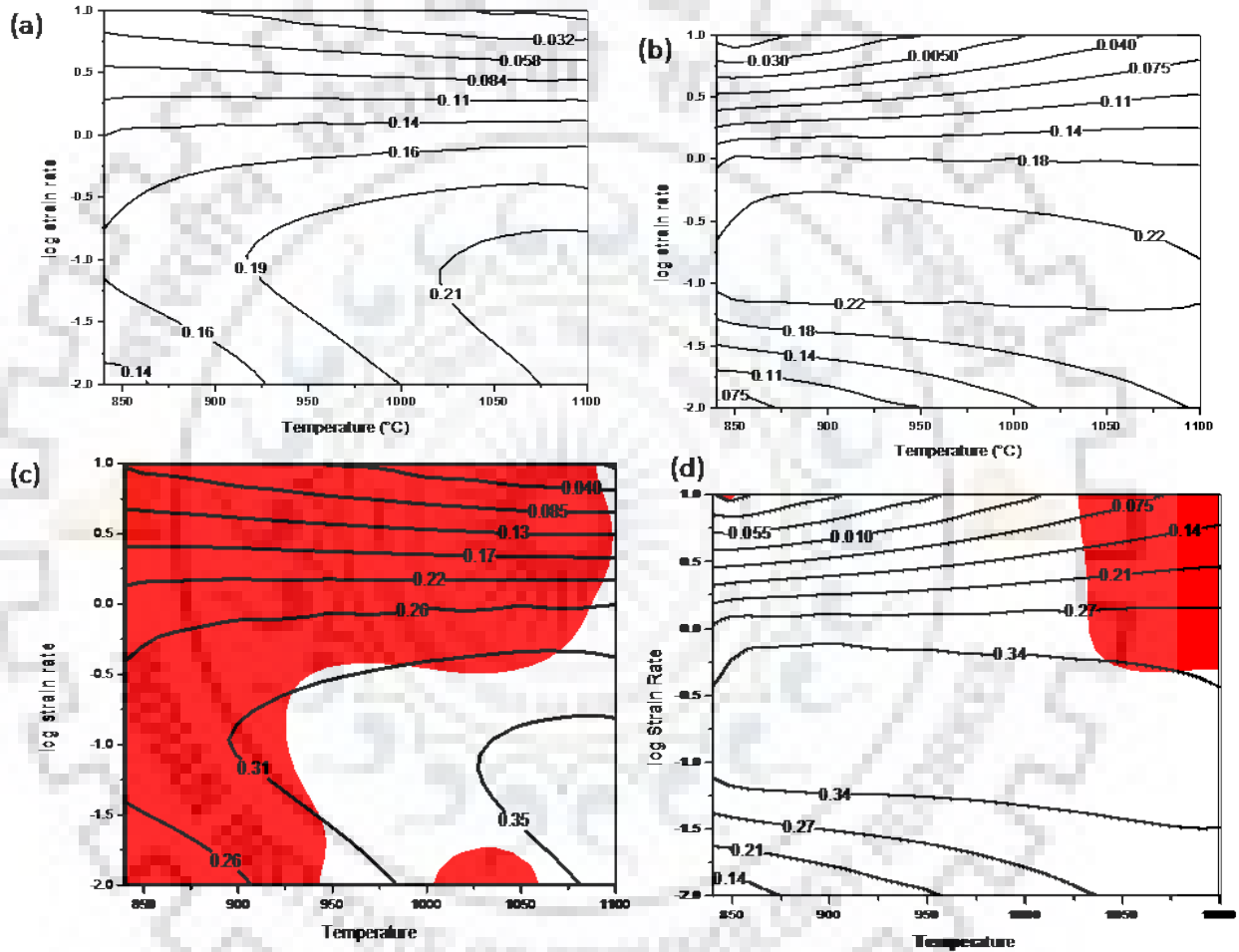


Fig. 5.12 Processing maps developed as a function of strain rate and deformation temperature (°C) for strain of 0.3 (left) and 0.6 (right). (a) and (b) strain sensitivity maps, (c) and (d) DMM based maps.

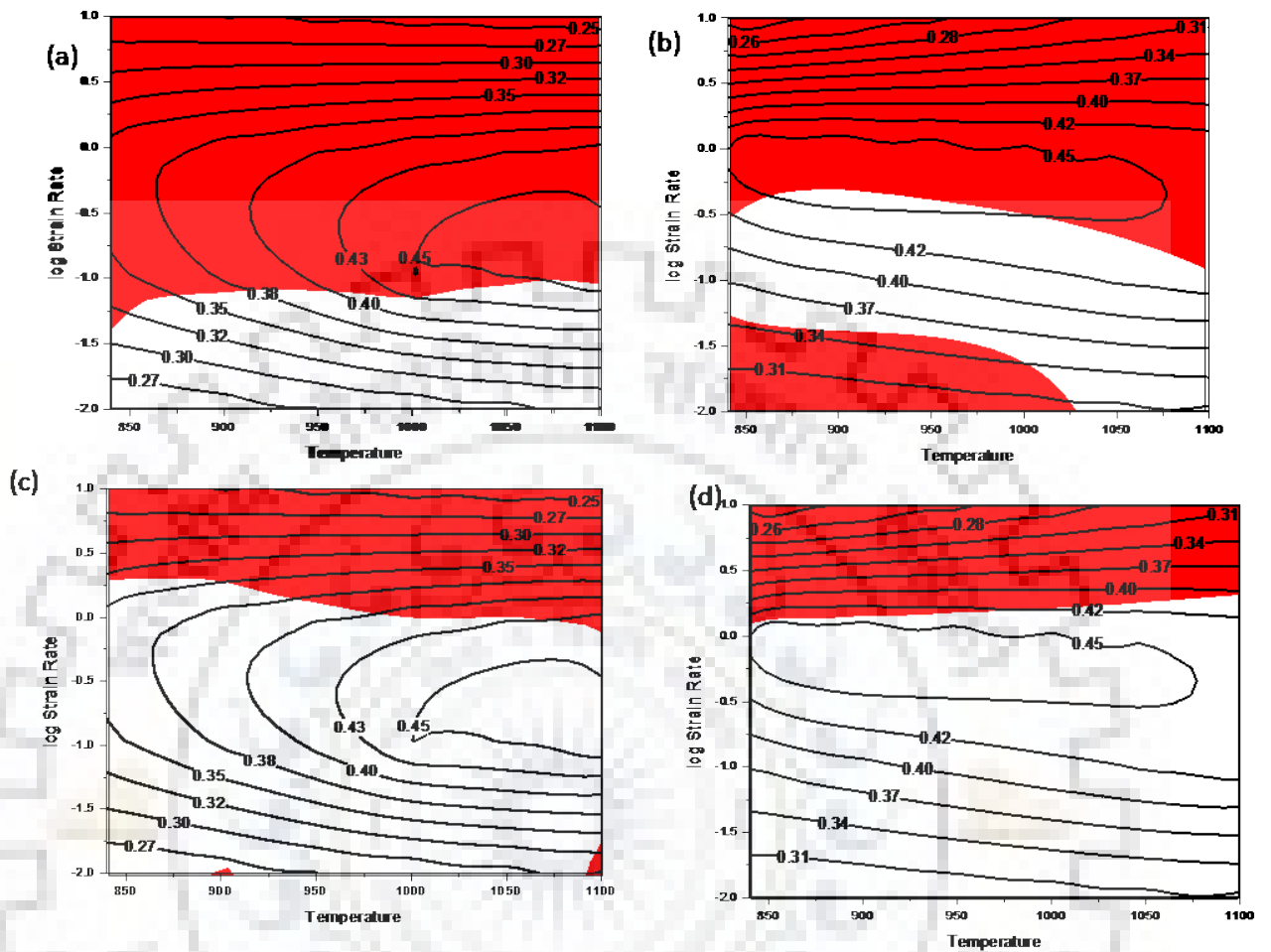


Fig. 5.13 Processing maps developed and plotted on scale of strain rate and deformation temperature($^{\circ}\text{C}$) for strain of 0.3 (left) and 0.6 (right). (a) and (b) modified DMM based maps, (c) and (d) modified DMM efficiency and instability parameter of Polletti[23]

5.7 Characterization of the hot deformed specimen

The deformed sample are cut along the center of compression axis into two semi-cylindrical parts and then mounted by using epoxy resin for the ease of metallography. The schematic diagram of the cut sample and area of interest for metallography is shown in Fig. 5.14. To avoid the effect of friction and dead and bulged zone in deformed specimen region near the centre is chosen for metallography. The optical micrographs of specimens after quenching by water spray of high carbon low alloy steel after hot compression tests at 900°C and 1100°C are shown in Fig. 5.15 and Fig. 5.16. Microstructure primarily consists of martensite and ferrite. Strain induced ferrite also contributes in increasing the ferrite content.

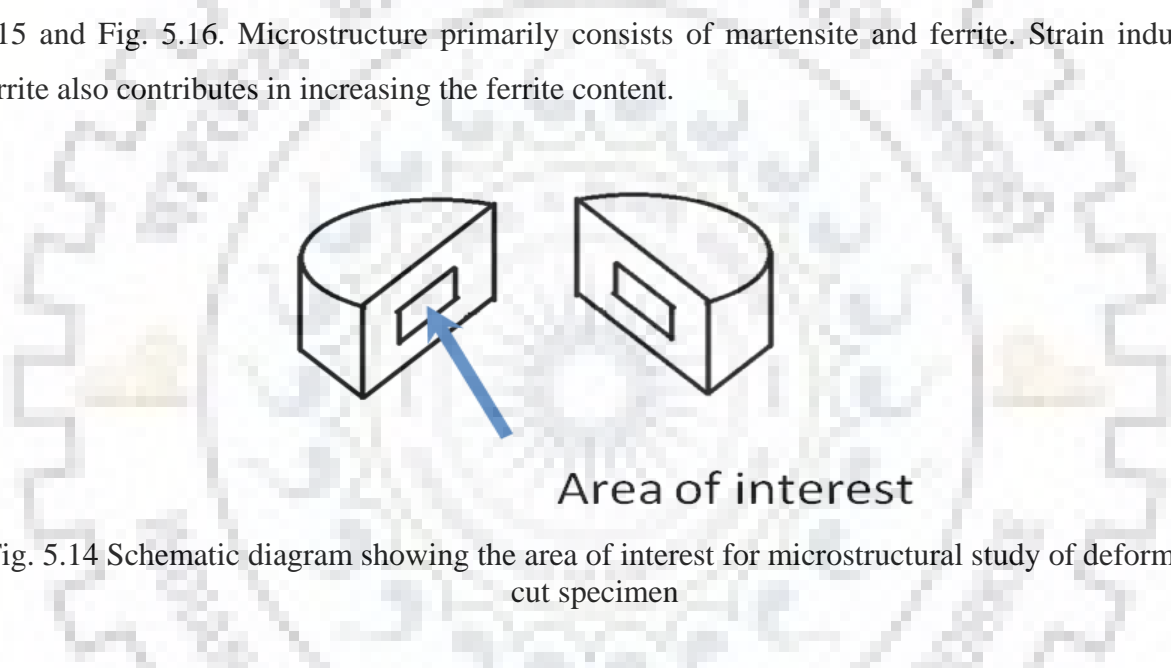


Fig. 5.14 Schematic diagram showing the area of interest for microstructural study of deformed cut specimen

It is observed from the light optical micrographs that all the specimen have martensitic microstructure (dark) and ferrite phase (bright) with varying amount of ferrite. At lower strain rate laths of martensite were observed while at higher temperature sharp needle like martensite is observed. The amount of bright region observed is higher at lower temperature. This indicates that some amount of ferrite is also formed during cooling from holding temperature. Additionally, some amount of ferrite also formed due to deformation called as deformation induced ferrite.

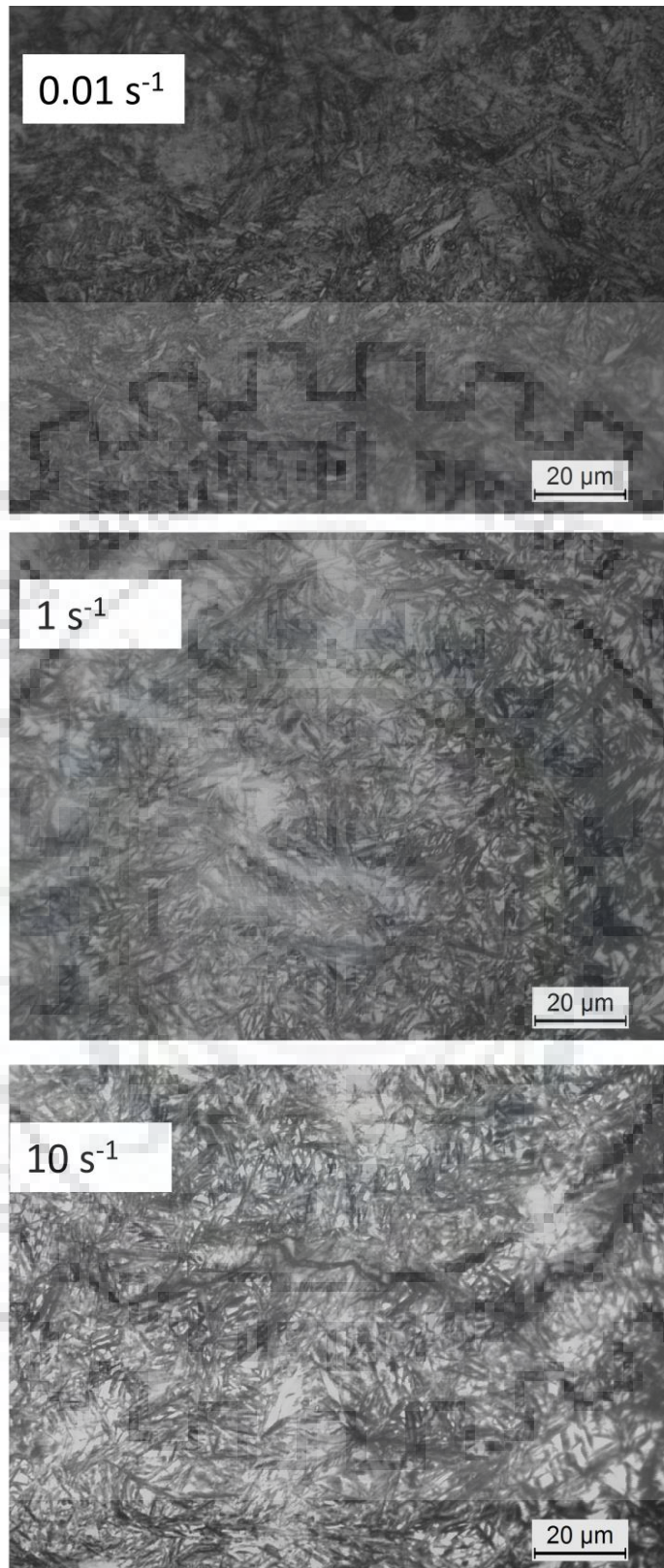


Fig. 5.15 optical micrographs of high carbon low alloy steel after deforming at 900°C showing ferrite(bright) and martensite (dark).A crack can be observed in micrograph of sample deformed at 10 s⁻¹

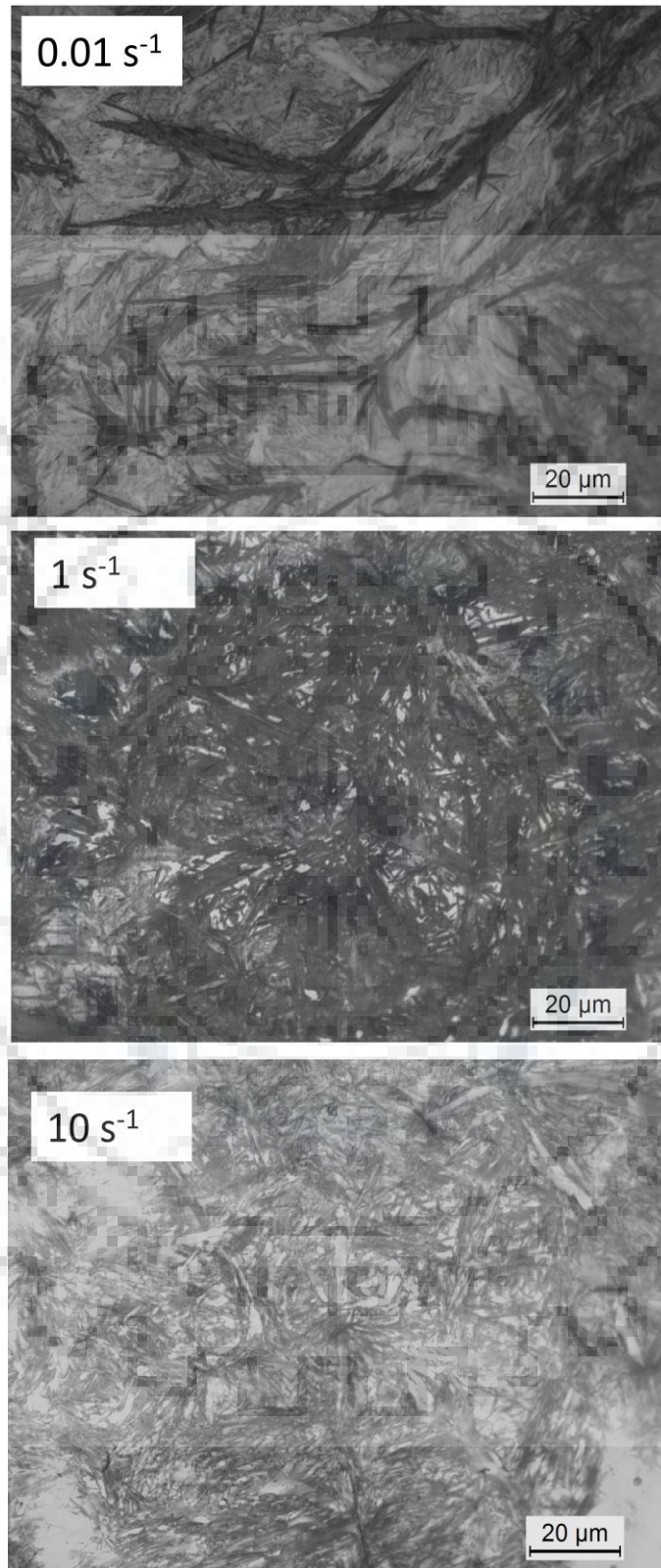


Fig. 5.16 Optical micrographs of high carbon low alloy steel after deforming at 1100°C

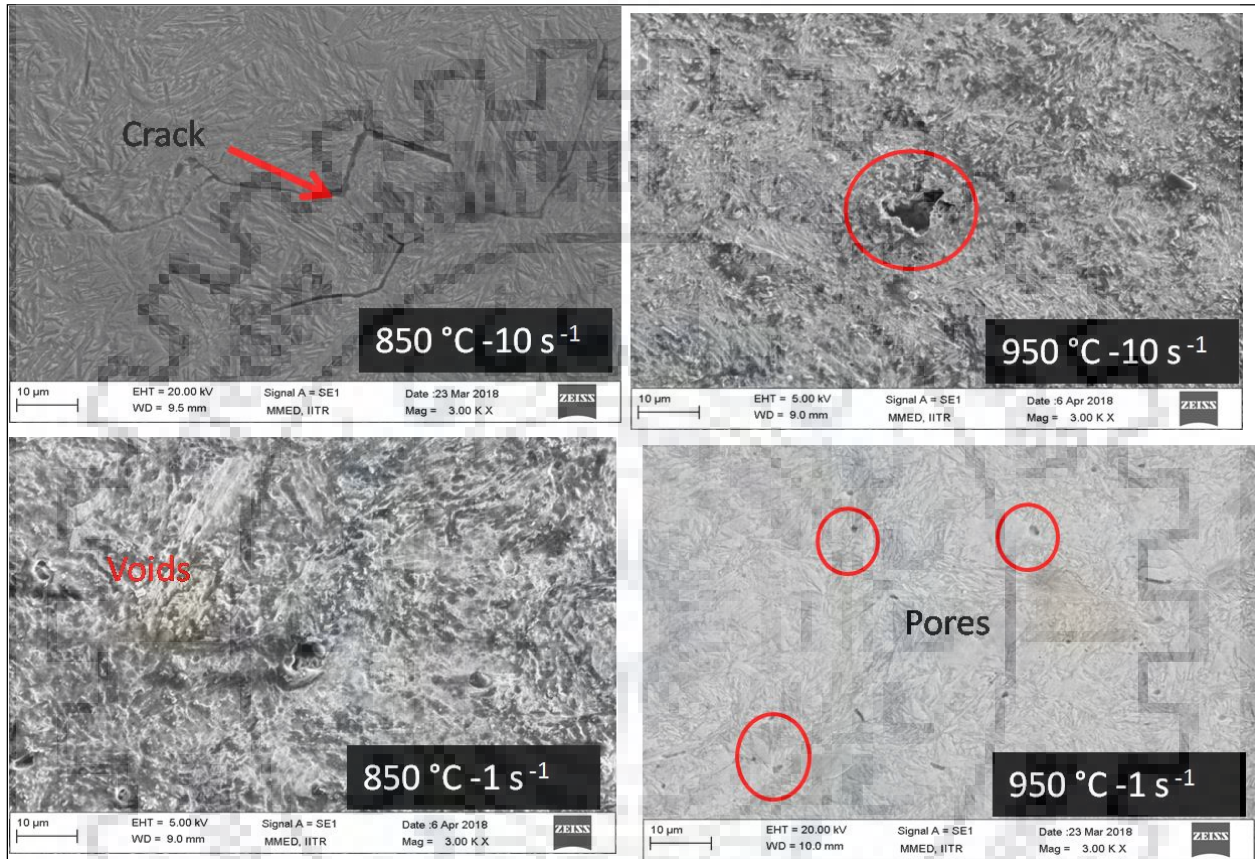


Fig. 5.17 SEM micrographs of steel specimen after hot compression showing various defects

The SEM micrographs as shown in Fig. 5.17 show the presence of various defects such as cracks, pores and voids. At low temperature and high strain rate severe defects in the form of long cracks are observed. While for strain of 1s^{-1} voids are observed.

CHAPTER 6 Artificial Neural Networks

Artificial Neural Network can prove to be a very useful tool in predicting the material behaviour in variable conditions. There is no requirement of any mathematical model to estimate the output rather it learns if there is any pattern in given data in repeated runs. Then it applies that to new data to predict whole output. Artificial Neural Network are made up of fundamental units known as nodes similar to the enormous network of neurons in a human brain. These artificial neurons are connected with synapses. Each node is fed with some inputs and output of each artificial neuron is calculated by non-linear function of the weighted sum of its inputs. Each connection is assigned a weight initially but values of these weights adjust itself as the learning progresses.

Flow behaviour of high carbon low steel estimated by developing a feed-forward back propagation algorithm with Lavenberg- Marquardt (L-M) training algorithm. Back propagation method progressively decreases the mean squared error between estimated output and targeted output. Training function was optimised using ‘Trainlm’ function to adjust the weights. The present model consists of three different layers consisting of input layer, output layer and a hidden layer.

Training of the network was carried out by using temperature. Strain rate and true strain as input data while experimental flow stress as output data. Trial and error method can be used to decide the number of neurons in hidden layer. However, the number of neurons in hidden layer can also be calculated using equation from Nworks Professional II Plus as:

$$h = \frac{\text{no.of training sets}}{m+n} \quad (6.1)$$

where h is the number of neurons in hidden layer, m is the number of neurons in input layer and n is the number of neurons in output layer. A total of 288 data points were used for modelling. After repeatedly runs by altering the number the neurons in hidden layer, it was found that minimum RMS value occurs for ten hidden neurons.

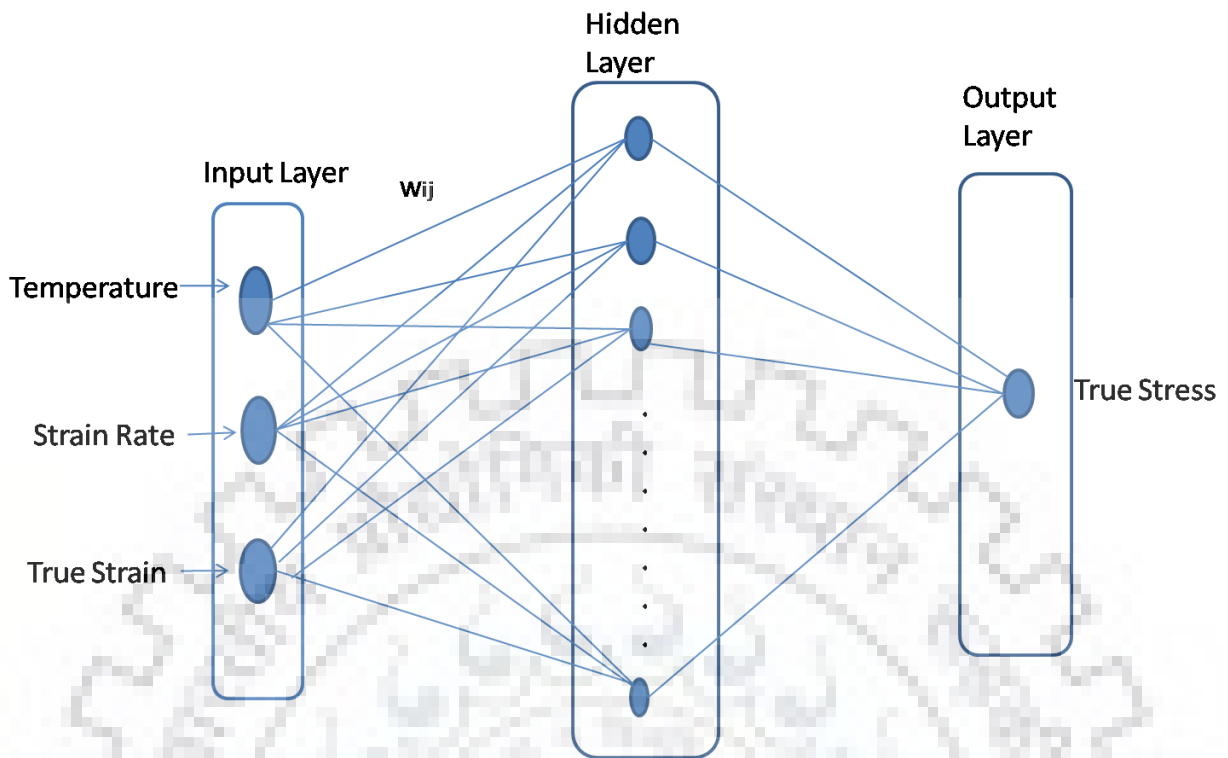


Fig. 6.1 Artificial Neural Network Model

6.1 Results of ANN modelling

Flow stress predicted by ANN for different strain rate was plotted on experimental flow curves. ANN predicted flow stress showed very good correlation which was further verified by calculating relative error (RE) as:

$$RE = \left(\frac{E_i - P_i}{E_i} \right) * 100\% \quad (6.2)$$

Where E_i and P_i are experimental and predicted value of flow stress. The relative errors were found in the range of 2.1%.

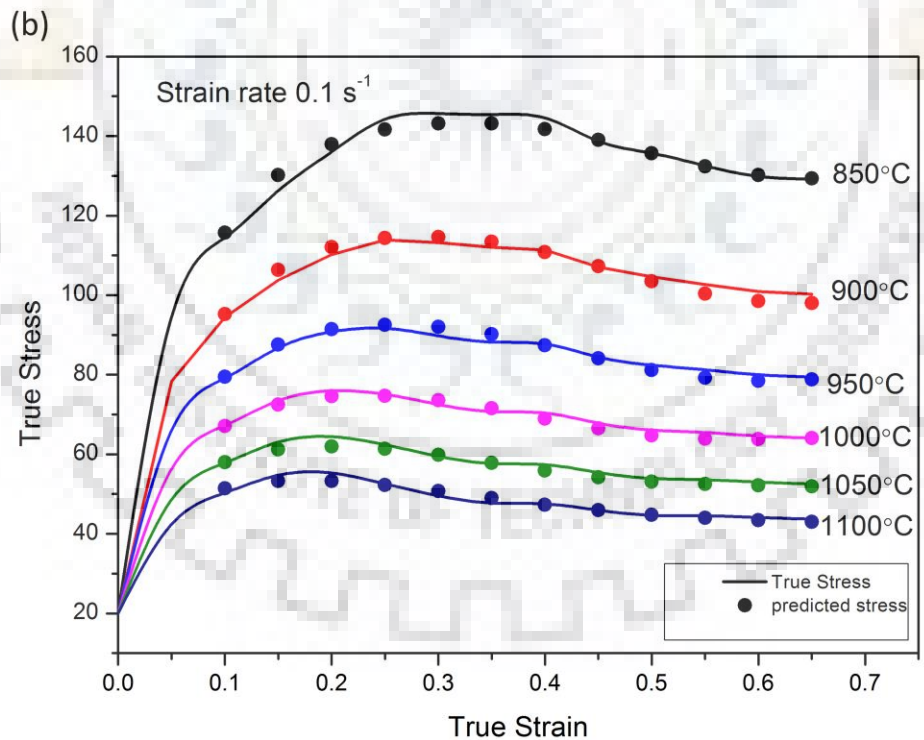
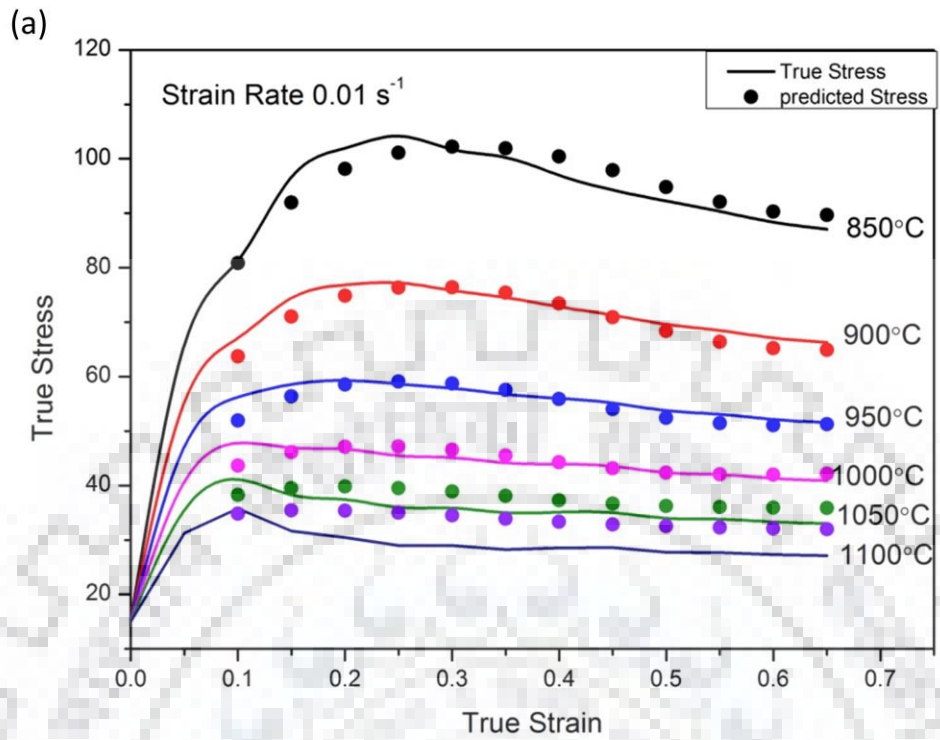


Fig. 6.2 Comparison between the experimental and predicted flow stress (MPa) by ANN model at different strain rates and temperatures (a) 0.01 s^{-1} (b) 0.1 s^{-1}

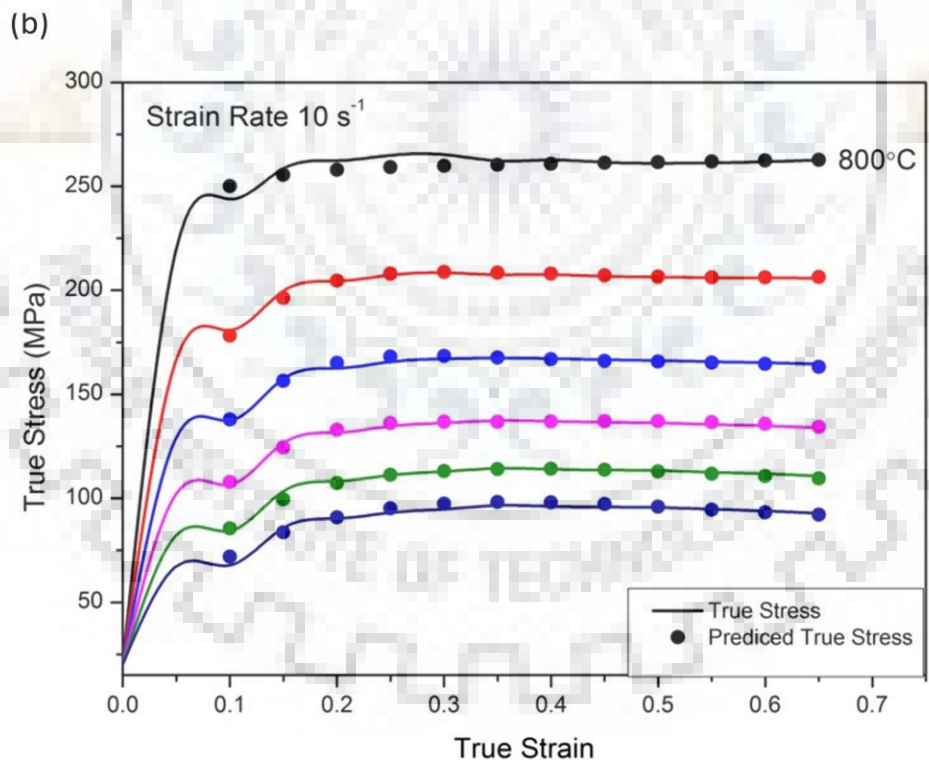
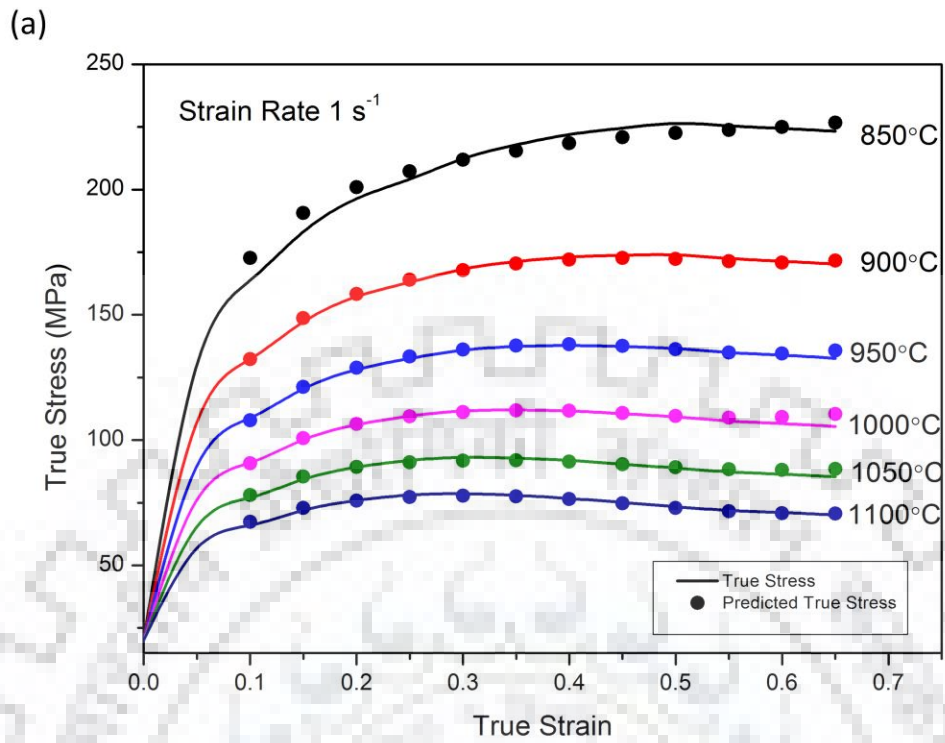


Fig. 6.3 Comparison between the experimental and predicted flow stress by ANN model at different strain rates and temperatures (a) 1 s^{-1} (b) 10 s^{-1}

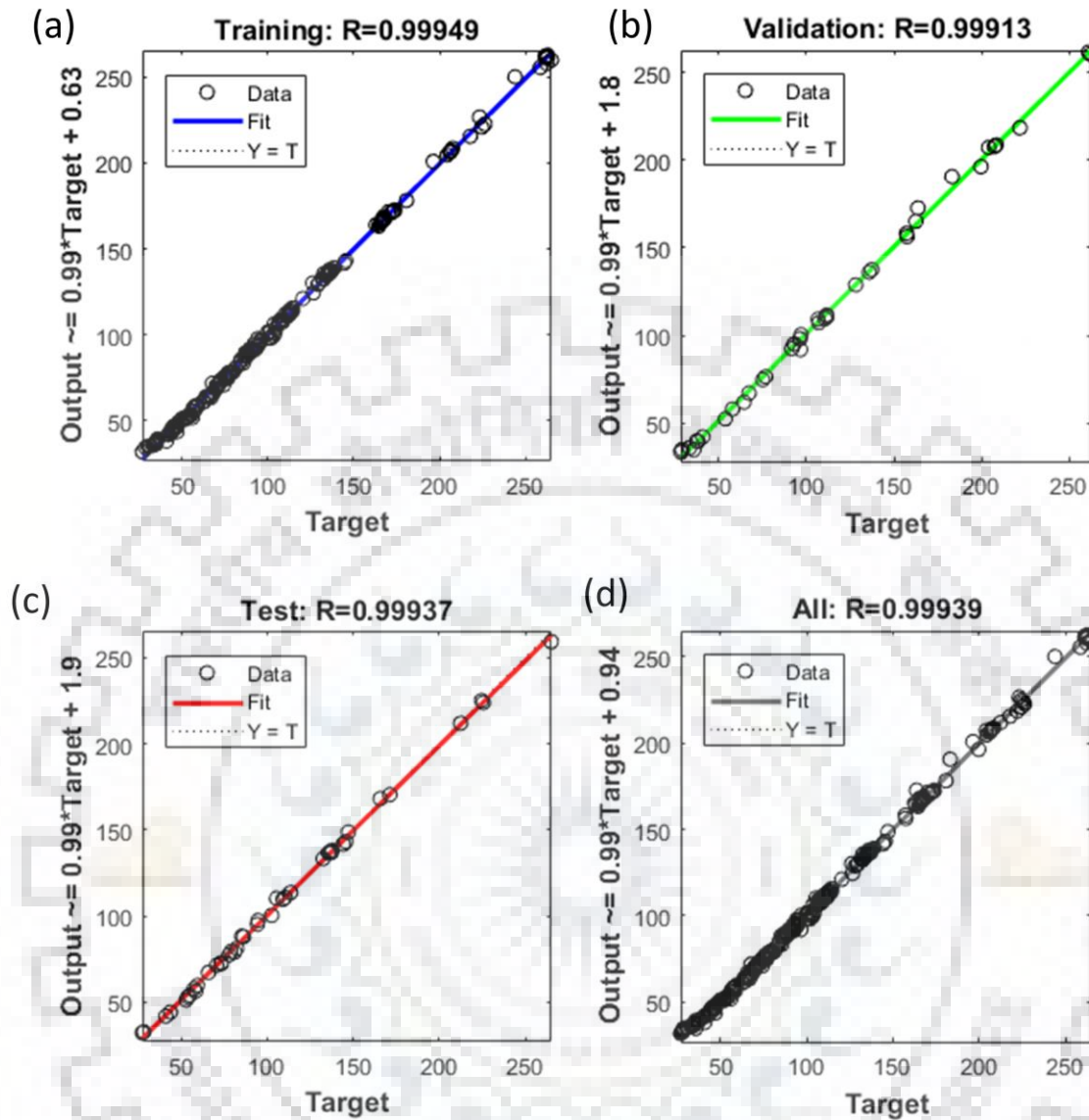


Fig. 6.4 Comparison between experimental flow stresses and calculated flow stresses: (a) Training data points (b) Validation data points (c) Test data points (d) All data points

The comparison between predicted and experimental stress is shown in Fig. 6.2 and Fig. 6.3. As can be seen most of the predicted stress values are well superimposed on experimental flow stress. Different types of data used in ANN are shown in Fig. 6.4. For exact prediction, all the data points should lie perfectly on line. From Fig 6.5 (a) it can be inferred that the well trained ANN shows good prediction ability.

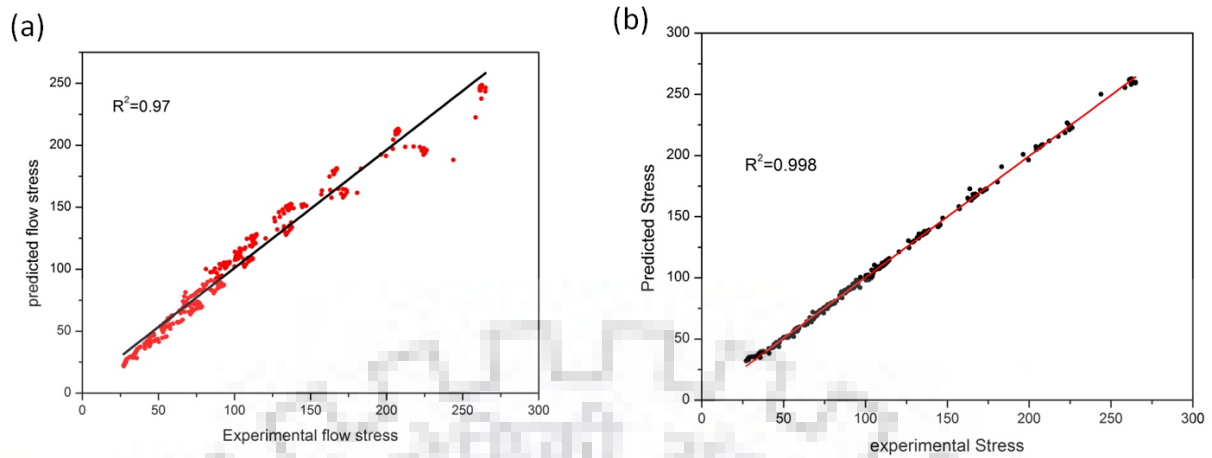


Fig. 6.5 Comparison of flow stress (MPa) predicted by (a) Constitutive modelling (b) ANN Modelling

Fig. 6.5 shows the comparison between modelling by constitutive equations and ANN model. It is clearly observed that ANN model gives better fitting and can be used in determining the hot workability of this steel. Further, better predictability by ANN can be confirmed by mean absolute error which is 2.1% in ANN model, while it was found to be 7.2% in case of constitutive modelling.

CHAPTER 7 Determination of critical conditions for Dynamic Recrystallisation

True Stress- True strain curves for strain rate of $0.01 - 1 \text{ s}^{-1}$ in temperature range $900-110 \text{ }^\circ\text{C}$ showed distinct peak which confirmed dynamic recrystallisation(DRX). Data for these curves was used for the calculation of critical condition of dynamic recrystallisation. First the experimental data was fitted with a nine degree polynomial because experimental data showed less smoothness which causes irregularities in differential curve and affect the analysis.

Ryan and McQueen[4] found that peak stress is found out at the point where strain hardening rate becomes zero. Then the derivative of strain hardening rate with respect to stress is plotted. The maximum point on these points represents the critical stress. Critical Strain can be found by looking for the strain corresponding to the critical stress in stress-strain data.

Fig. 7.1 shows the variation of strain hardening rate versus stress. The point corresponding to zero strain hardening rate represent peak stress. Below zero the curve shows the strain softening zone. At strain rate of 0.01 s^{-1} it can be observed that θ value again touches the zero line signifying the completion of one cycle of completion of DRX. The value of peak stress increases with increase of strain rate.

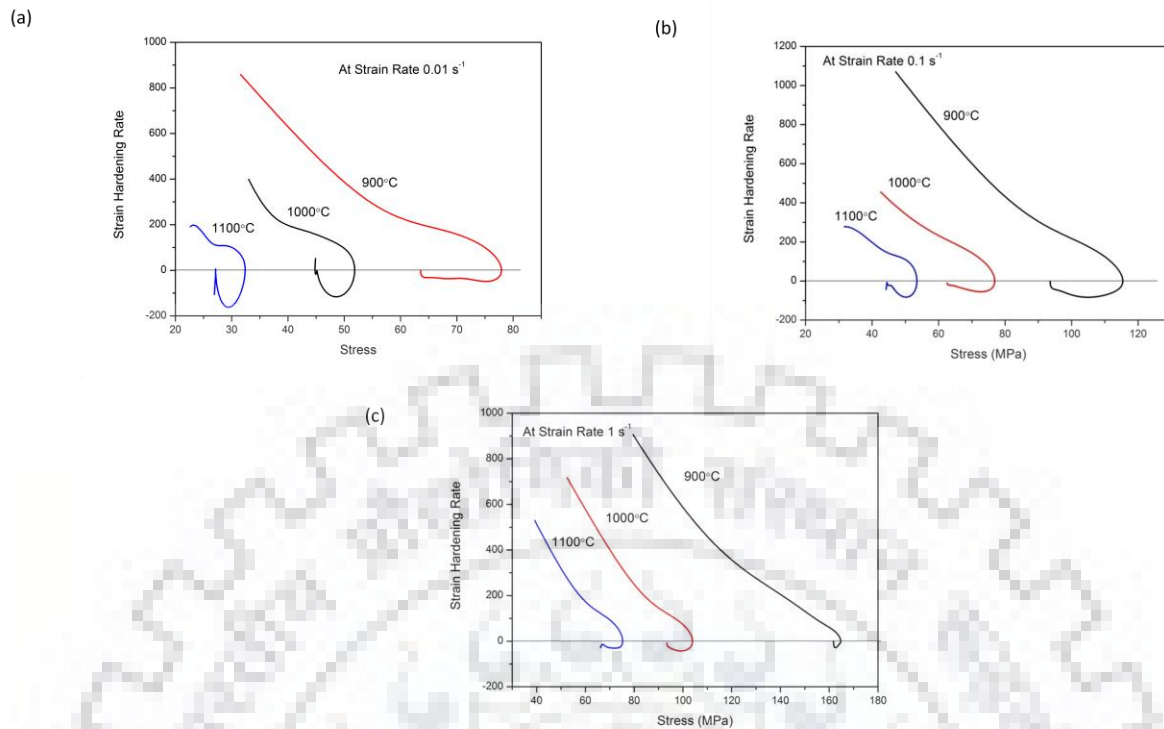


Fig. 7.1 Strain hardening rate (θ) versus true stress at (a) 0.01 s^{-1} (b) 0.1 s^{-1} (c) 1 s^{-1}

7.1 Strain for maximum dynamic softening

The minimum points on the work hardening rate vs strain rate represent the strain for dynamic softening (ϵ^*). It is observed that value of ϵ^* increases with decreasing deformation temperature and increasing strain rate. From θ - ϵ plots it can be observed that 1100°C , there is completion of dynamic recrystallisation. However, at 900°C there is partial dynamic recrystallisation for all strain rate.

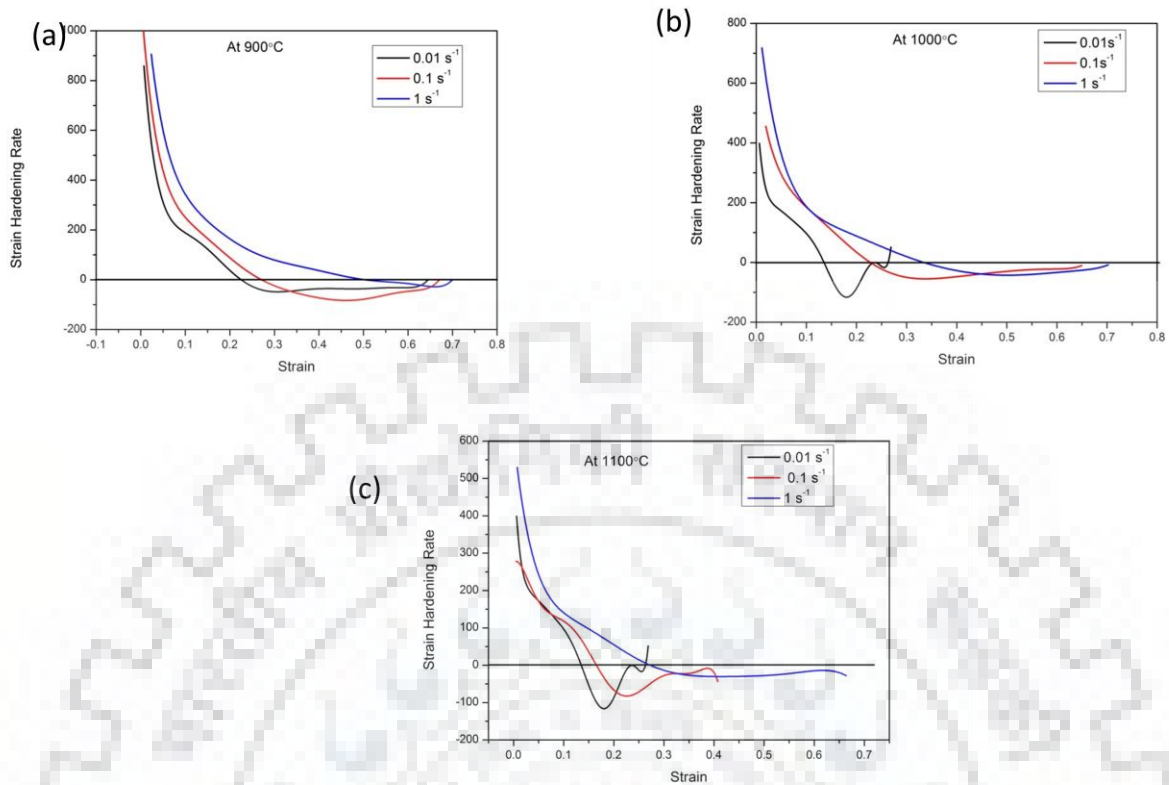


Fig. 7.2 Strain hardening versus strain at (a) 900°C (b) 1000°C (c) 1100°C

From the data given in Fig. 7.1 the derivative of strain hardening rate ($d\theta/d\sigma$) as a function of flow stress for various strain rates and temperature was estimated. The $d\theta/d\sigma$ versus σ plots are given in Fig. 7.3. The maximum point in these curves represents the critical stress. The strain corresponding to critical stress is critical strain.

It can be inferred from the Fig. 7.2 that at lower strain rate and higher temperature, Softening occurs earlier while it is delayed for higher strain rate and lower temperature. This confirms the occurrence of cyclic DRX at low strain rate and higher temperature. It can be observed from the curve of strain hardening rate for 0.01 s⁻¹ at 1100°C becomes zero for true strain of 0.25. Then again it goes in positive region showing the onset of second DRX cycle.

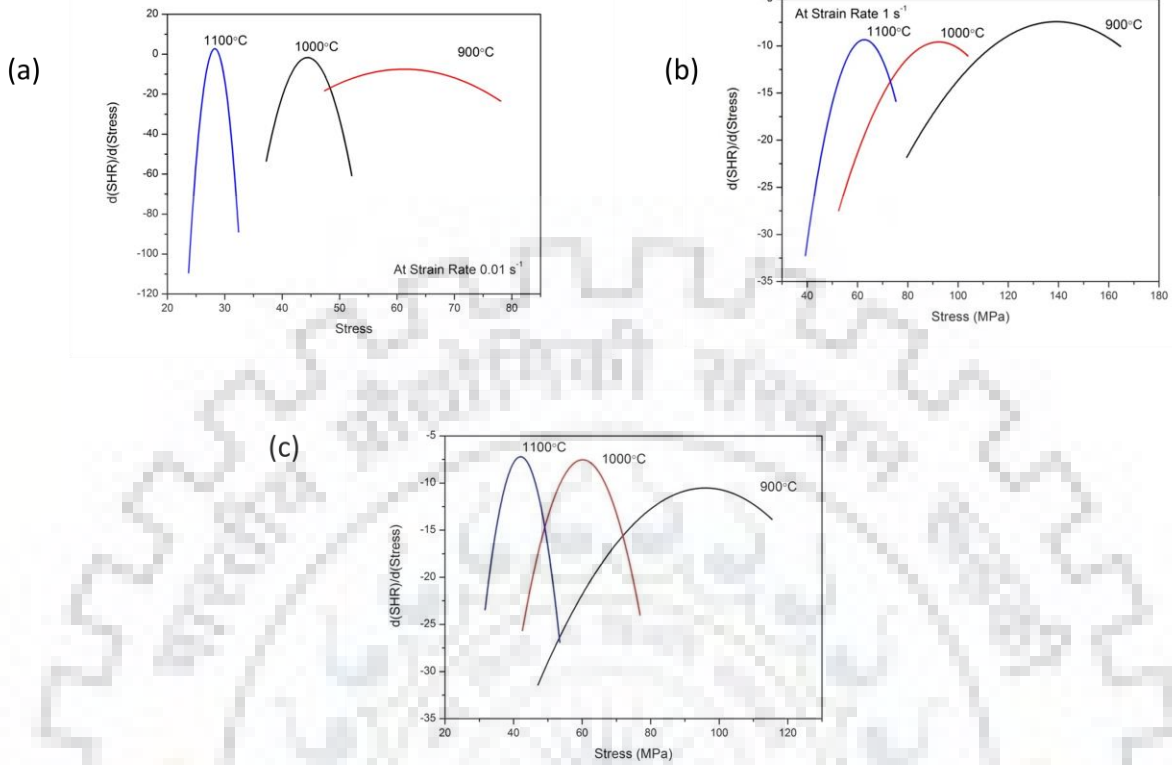


Fig. 7.3 Curves of $d\theta/d\sigma$ versus σ at strain rate of (a) 0.01 s^{-1} (b) 0.1 s^{-1} (c) 1 s^{-1}

7.2 Extent of Dynamic Recrystallisation

Avrami type model can describe the extent of dynamic recrystallisation in terms of volume fraction as follows:

$$X_{DRX} = 1 - \exp\left(-0.693 \left(\frac{\varepsilon - \varepsilon_c}{\varepsilon^* - \varepsilon_c}\right)^2\right) \quad (6.1)$$

Where X_{DRX} is the fraction of dynamic recrystallisation, ε is the true strain, ε^* is the strain for the maximum dynamic softening rate and ε_c is the critical rate for onset of dynamic recrystallisation. It is seen that volume of dynamic recrystallisation reaches a value of 1 for the 100% dynamic recrystallisation. As temperature is decreased strain required for reaching specified amount of DRX is increased. Further, the onset of steady state could be identified from the plot of work hardening rate vs strain. As the work hardening rate approaches zero, the steady state said to have been achieved.

It can be confirmed that Avrami model shows good predictability of extent of dynamic recrystallisation which can be inferred from its coincidence with work hardening rate vs strain plot.

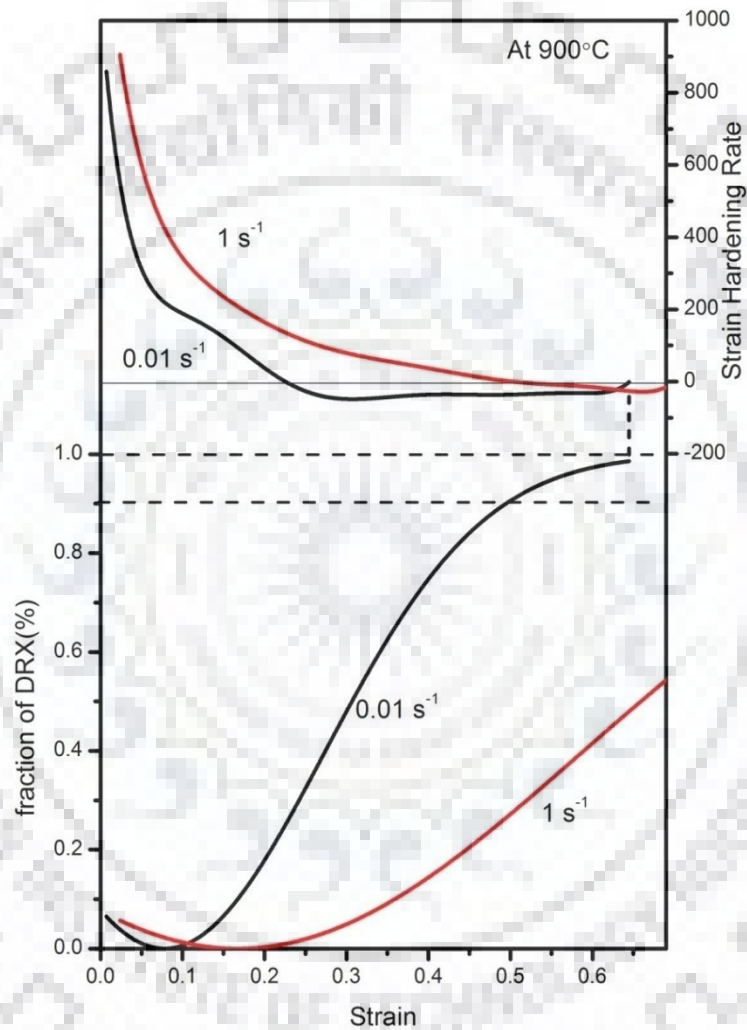


Fig. 7.4 Coincidence of predicted steady state strain with work hardening rate and with the model used for calculation of recrystallized fraction. showing nearly 98% DRX for 0.01 s⁻¹

while partial DRX is confirmed by 1 s⁻¹ showing 53% DRX

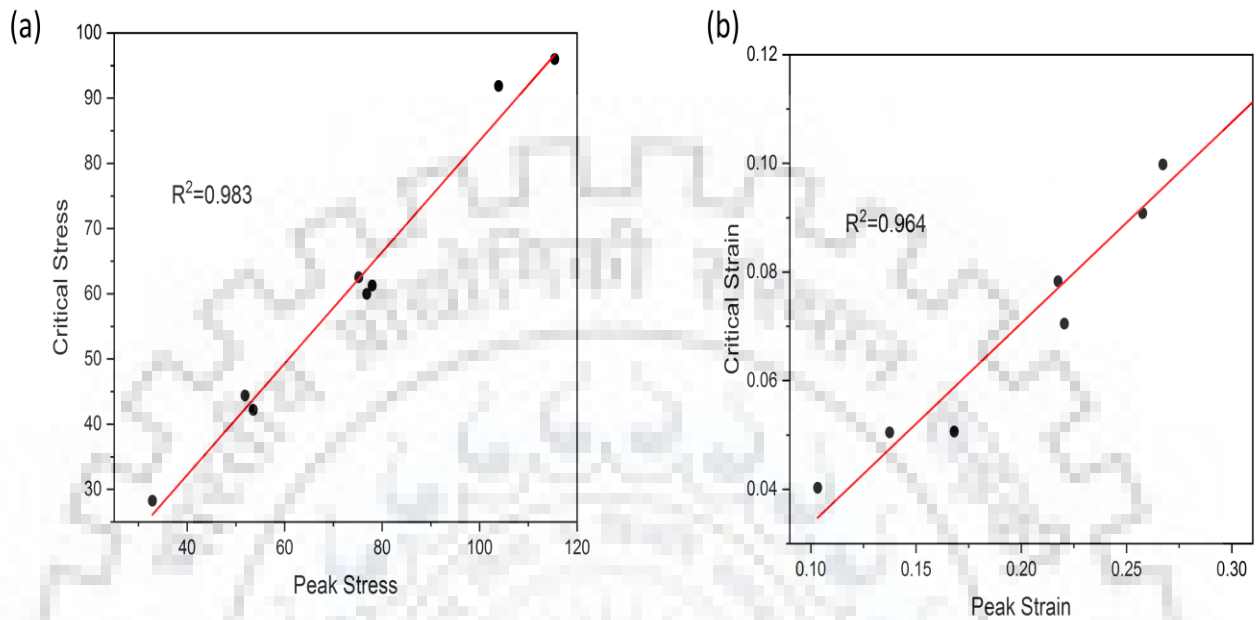


Fig. 7.5 Correlation between (a) critical stress and peak stress (b) critical strain and peak strain

Fig. 7.5 shows the relationship between critical stress and strain with peak stress and strain. It shows the critical stress is a linear function of peak stress. Similar is the case critical strain. In that case constitutive models used to find the peak stress can be comfortably applied to find the critical stress.

CHAPTER 8 Summary

The hot deformation behaviour of high carbon low alloy steel is analysed in the temperature range of 850°C – 1100°C and in strain rate range of 0.01 s⁻¹ to 10 s⁻¹ for the total deformation of true strain 0.69. Flow behaviour of steel is modelled using constitutive modelling. Processing maps based on DMM, Modified DMM and modified DMM using Poletti criteria were developed. A model based on Artificial Neural Network (ANN) is also developed to predict the flow behaviour.

Critical parameters for onset of DRX are also calculated with fraction of DRX using Avrami type of model. After proper study and analysis of obtained results, following conclusion are drawn from the study.

1. At lower strain rate and higher temperature both power dissipation efficiency and strain rate sensitivity are maximum. This is attributed to the occurrence of phenomena of Dynamic restoration such as DRX and DRV.
2. Adiabatic temperature rise is high at higher strain rate as compared lower strain rate. This is observed because there is very less time available for heat dissipation because of very high deformation rate.
3. For lower values of Z-parameter high amount of softening is observed due to DRX and DRV.
4. All the material constants are found and fitted with five degree polynomial to show the variation with true strain.
5. There is a very good conformity found between predicted and experimental flow stress. This verifies the constitutive model.
6. As a general trend it is observed that instability region shrinks with increasing strain which can be attributed to the fact that for longer deformation the stress value becomes constant and hardening-softening cycles cease to exist.
7. Metallographic investigations showed the variety of instabilities like crack, voids, pores and adiabatic shear bands confirming the instable region predicted by the processing maps.

8. Stress predicted by ANN model is in close agreement with the experimental data. Correlation coefficient (R^2) was found to be 0.999 which confirms the very good predictability of flow behaviour by ANN.
9. Critical strain for onset of DRX was for the temperature of 900°C, 1000°C, 1100°C for the strain rate of 0.01, 0.1, 1 s⁻¹.
10. Strain hardening rate vs stress curves were plotted to know about peak stress, maximum strain softening rate.
11. Fraction of amount of DRX occurred during deformation was calculated using the Avrami type of model. It showed good agreement with experimental data.
12. Correlation coefficient between critical stress and peak strain is found to be 0.98 which confirms that critical stress closely follows the peak strain.



CHAPTER 9 Future scope of work

In the present work, the hot deformation behaviour of high carbon low alloy steel was studied in the temperature range of 850°C-1100°C and in strain rate range of 0.01-10 s⁻¹. In the continuation of study, it can be further analysed in wider domain of temperature and strain rate. Processing maps can be developed for each true strain starting from 0.1 up to 0.65 s⁻¹. Then Evolution of processing maps with true strain can be studied. ANN model can be developed using more data points to predict behaviour accuracy. The critical parameters for onset of DRX can be calculated for all temperature to find a pattern for high carbon low alloy steel.



References:

- [1] Dieter G E, Kuhn H a. and Semiatin S L 2003 Handbook of Workability and Process Design *Handb. Work. Process Des.* 278–90
- [2] Prasad Y V R K and Seshacharyulu T 1998 Modelling of hot deformation for microstructural contro *Int. Mater. Rev.* **43** 243–58
- [3] Murty S V S N and Rao B N 1998 On the development of instability criteria during hotworking with reference to IN 718 *Mater. Sci. Eng. A* **254** 76–82
- [4] Ryan N D and McQueen H J 1990 Dynamic softening mechanisms in 304 austenitic stainless steel *Can. Metall. Q.* **29** 147–62
- [5] Rastegari H, Kermanpur A, Najafizadeh A, Porter D and Somani M 2015 Warm deformation processing maps for the plain eutectoid steels *J. Alloys Compd.* **626** 136–44
- [6] Zhang J, Kwon H C, Kim H Y, Byon S M, Park H D and Im Y T 2005 Micro-cracking of low carbon steel in hot-forming processes *J. Mater. Process. Technol.* **162–163** 447–53
- [7] Rastegari H, Kermanpur A, Najafizadeh A, Somani M C, Porter D A, Ghassemali E and Jarfors A E W 2016 Determination of processing maps for the warm working of vanadium microalloyed eutectoid steels *Mater. Sci. Eng. A* **658** 167–75
- [8] Ebrahimi G R, Momeni A, Kazemi S and Alinejad H 2017 Flow curves, dynamic recrystallization and precipitation in a medium carbon low alloy steel *Vacuum* **142** 135–45
- [9] Yang Z, Zhang F, Zheng C, Zhang M, Lv B and Qu L 2015 Study on hot deformation behaviour and processing maps of low carbon bainitic steel *Mater. Des.* **66** 258–66
- [10] Zhang C, Zhang L, Shen W, Liu C, Xia Y and Li R 2016 Study on constitutive modeling and processing maps for hot deformation of medium carbon Cr-Ni-Mo alloyed steel *Mater. Des.* **90** 804–14
- [11] Zhang Z, Zhou H, Liu X, Li S, Dong J, Si G, Zhang B and Yue S 2013 Hot deformation behavior and processing maps for coiled tubing steel *Mater. Sci. Eng. A* **565** 213–8
- [12] Rajput S K, Chaudhari G P and Nath S K 2016 Characterization of hot deformation behavior of a low carbon steel using processing maps, constitutive equations and Zener-Hollomon parameter *J. Mater. Process. Technol.* **237** 113–25
- [13] Rajput S K, Dikovits M, Chaudhari G P, Poletti C, Warchomicka F, Pancholi V and Nath

- S K 2013 Physical simulation of hot deformation and microstructural evolution of AISI 1016 steel using processing maps *Mater. Sci. Eng. A* **587** 291–300
- [14] Babu K A, Mandal S, Athreya C N, Shakthipriya B and Sarma V S 2017 Hot deformation characteristics and processing map of a phosphorous modified super austenitic stainless steel *Mater. Des.* **115** 262–75
- [15] Ma X, An Z, Chen L, Mao T, Wang J, Long H and Hongyan X 2015 The effect of rare earth alloying on the hot workability of duplex stainless steel - A study using processing map *Mater. Des.* **86** 848–54
- [16] Pu E, Zheng W, Xiang J, Song Z and Li J 2014 Hot deformation characteristic and processing map of superaustenitic stainless steel S32654 *Mater. Sci. Eng. A* **598** 174–82
- [17] Wang L L, Li R B, Liao Y G and Jin M 2013 Study on characterization of hot deformation of 403 steel *Mater. Sci. Eng. A* **567** 84–8
- [18] Ji G, Li F, Li Q, Li H and Li Z 2010 Development and validation of a processing map for Aermet100 steel *Mater. Sci. Eng. A* **527** 1165–71
- [19] Singh K, Rajput S K and Mehta Y 2016 Modeling of the hot deformation behavior of a high phosphorus steel using artificial neural networks *Mater. Discov.* **6** 1–8
- [20] YAN J, PAN Q lin, LI A de and SONG W bo 2017 Flow behavior of Al–6.2Zn–0.70Mg–0.30Mn–0.17Zr alloy during hot compressive deformation based on Arrhenius and ANN models *Trans. Nonferrous Met. Soc. China (English Ed.)* **27** 638–47
- [21] Shaban M and Eghbali B 2010 Determination of critical conditions for dynamic recrystallization of a microalloyed steel *Mater. Sci. Eng. A* **527** 4320–5
- [22] Raj R 1981 Development of a Processing Map for Use in Warm-Forming and Hot-Forming Processes *Metall. Trans. A* **12** 1089–97
- [23] Poletti C, Großeiber S, Llie S and Degischer H P 2011 Hot deformation behaviour of low alloyed steel *Mater. Sci. Forum* **706–709** 2794–9
- [24] Frost H. J. A M F 1982 Deformations mechanism maps *Pergamon, New York* **1**
- [25] Ziegler H " 1963 *Progress in solid mechanics.*" Ed. Sneddon, IN y Hill, R., Nueva York vol 4
- [26] Montheillet F, Lépinoux J, Weygand D and Rauch E 2001 Dynamic and static recrystallization *Adv. Eng. Mater.* **3** 587–9
- [27] C. Sellars and W. M. Tegart: 1966 On the mechanism of hot deformation *Acta Met.* 1136–1138

